TECHNISCHE UNIVERSITÄT WIEN

Diploma Thesis

ELASTO-PLASTIC FINITE ELEMENT SIMULATIONS OF NANOINDENTATION PROBLEMS UTILIZING HILL'S POTENTIAL

carried out for the purpose of obtaining the degree of Master of Science (MSc or Dipl.-Ing), submitted at TU Wien, Faculty of Mechanical and Industrial Engineering, by

Paul HOFFMANN

Mat.Nr.: 1027168

Schönbrunnerstraße 149

1050 Wien

under the supervision of

Associate Prof. Dipl.-Ing. Dr. techn. Heinz Pettermann

Dipl.-Ing. Dr. techn. Martin Springer

Institute of Lightweight Design and Structural Biomechanics

reviewed by

Heinz Pettermann

ILSB, E317

Paul Heinz Mayrhofer

WWWT, E308

Acknowledgment

Contents

Abstract

To enable a reliable application of semiconductor devices based on single crystal Gallium Nitride (GaN), knowledge about their electrical and mechanical performance is important. Numerical simulations within the framework of the finite element method (FEM) can help to enhance or clarify results of common mechanical testing procedures like nanoindentation experiments. To conduct such simulations, it is necessary to understand the mechanical behavior of GaN and to use the appropriate modeling approach.

The main goal of this thesis is to generate a reasonable elasto-plastic FEM simulation of GaN nanoindentation experiments. In order to sufficiently reproduce the plasticity in the GaN, the parameters of the Hill's yield criterion are estimated according to the orientation and the critical shear stresses of the various slip systems of GaN. In combination with an appropriate set of transversely isotropic elastic parameters and a constant tangent modulus, this modeling approach is applied to axisymmetric and three-dimensional FEM models of nanoindentation experiments.

These models are used to evaluate the influence of material parameters and indenter shapes. Furthermore, the resolved shear stresses of various slip systems are examined with regard to the critical values. The results show a very good correlation to the sought experimental load-penetration curve, and the assessment of the stress state indicates slips in the expected slip systems. Overall, the approximation by Hill's potential works well for the studied GaN systems, circumventing complicated and computational expensive classic crystal plasticity approaches.

Kurzfassung

Um eine zuverlässige Anwendung von Halbleiterbauelementen auf der Basis von einkristallinem Galliumnitrid (GaN) zu ermöglichen, ist sowohl Wissen über die elektronische wie auch über die mechanische Leistungsfähigkeit derselben erforderlich. Numerische Simulationen mit der Finite-Elemente-Methode (FEM) können dabei unterstützend zu experimentellen Analysen verwendet werden. Um solche Simulationen durchzuführen zu können, ist Verständnis über das mechanische Verhalten von GaN und die Wahl des passenden Modellierungsansatzes von essentieller Bedeutung.

Das Hauptziel dieser Arbeit ist es daher, einen passenden Ansatz für das elasto-plastische Verhalten von GaN bei Nanoindentationsexperimenten zu erarbeiten. Um den Fließbeginn in der GaN-Schicht hinreichend abbilden zu können, werden auf Basis der Orientierungen und der kritischen Schubspannungen der einzelnen Gleitsysteme die Parameter der Hill'schen Vergleichsspannungshypothese definiert. In Kombination mit einem geeigneten transversal isotropen elastischen Materialgesetz und einem konstanten Tangentenmodul wird dieser Modellierungsansatz auf axialsymmetrische und dreidimensionale FEM-Modelle von Nanoindentationsexperimenten angewandt.

Diese Modelle werden anschließend verwendet, um den Einfluss verschiedener Materialparameter und Indentertypen zu evaluieren. Weiters werden die Schubspannungszustände der verschiedenen Gleitsysteme hinsichtlich ihrer kritischen Werte untersucht. Die Ergebnisse zeigen eine sehr gute Korrelation zwischen der simulierten und der angestrebten experimentellen Systemantwort. Auch treten kritische Schubspannungswerte in Gleitsystemen auf, in denen dies zu erwarteten ist. Somit ist nachgewiesen, dass sich die Approximation mittels dem Hill'schen Potenzial für die untersuchten GaN-Systeme eignet, wodurch eine Verwendung von komplizierten Kristallplastizitäts-Modellen umgangen wird.

Chapter 1

Introduction

Single crystal materials are commonly used in the semiconductor industry. Such materials share the same crystal orientation over the whole solid, which means that the elastic and plastic material properties are direction-dependent. It is difficult to model such a material in an elastic-plastic Finite Element Method (FEM) analysis because standard crystal plasticity models are complicated in the application and computationally expensive and classic continuum approaches like J2 plasticity do not take the anisotropy of the material into consideration.

In this thesis, an approach utilizing Hill's plasticity theory to model the plastic behavior of single crystals is presented. This approach is applied within FEM simulations of nanoindentation experiments. The probe in the modeled experiment is a wafer with a stack consisting predominantly of single crystal Gallium Nitride (GaN) on a Silicon substrate.

Such a wafer structure is interesting, because recent developments in GaN based technologies have shown that GaN-on-Silicon-based solutions possess extensive technological potential, utilized especially in high-power electronic devices [24]. This is due to the fact that GaN technologies have a higher energy efficiency and power density in a smaller footprint compared to similar Silicon-based products [14].

The mechanical properties of such GaN-on-Silicon wafers are quite difficult to obtain, however they are important to know for assessing their behavior during wafer processing, where thermo-mechanical stresses occur due to process-related temperature transients. A method of choice for mechanical thin film characterization is nanoindentation, which is commonly applied at the Kompetenzzentrum Automobil- und Industrieelektronik GmbH (KAI), Villach Austria.

1.1 Motivation

A sophisticated FEM analysis of such problems has the potential to save a lot of money and time because it allows to study the influence of different stack designs on the mechanical properties of the wafer, without having to explore all possible options by expensive processing experiments in the first place. Moreover, it would enable an in-depth analysis of the stress state and the plastic deformation.

1.1.1 Background Work

This thesis is the second one in a series of three. The first one, which is not yet published, is carried out by Clemens Reichel and concentrates on the topic of fracture mechanics. He has set up an FEM model to simulate crack propagation in brittle, multilayered structures focusing also on GaN-on-Silicon wafers. The crack initiation and propagation has been modeled utilizing cohesive zone elements and the material behavior has been assumed to be linear elastic without plasticity.

Reichel has been able to obtain significant results regarding the crack development. He has shown that residual stresses can have a very high influence on the crack-propagation behavior in the way that even relatively small residual stresses may lead to an unstable propagation of surface cracks. Without residual stresses, no similar surface cracks appear, rather there is stable crack propagation downwards.

Another finding has been that the predicted energy dissipation seen in the load-penetration curve is insignificant compared to the experimental result. The higher energy dissipation of the experiment has been attributed to material plasticity in the GaN layer. Reichel has also noticed the occurrence of shear stresses larger than 10 GPa in the GaN layer which is another indication for the occurrence of plasticity.

1.1.2 Aims and Objectives

The aims and objectives of this thesis can be divided into three tasks connected to each other. First, the plastic behavior of the GaN will be addressed by the introduction of Hill's plasticity theory. In order to apply this theory correctly, the plasticity mechanisms in GaN are identified and the resulting Hill plasticity behavior is verified through simple single element tests.

Second, this material model has to be combined with the appropriate elastic properties and then applied to a FEM model of nanoindentation experiments. During this step, different elastic material parameters and various other assumptions are tested and calibrated. Amongst other things, the influence of hardening behavior, isotropic and anisotropic elastic properties, residual stresses, indenter tip geometry, and plasticity in Silicon on the simulation are studied.

Lastly, the simulation of one of the experiments conducted at the KAI is studied in more detail. An analysis of the resolved shear stresses in the activated slip systems is done and the plastic region is determined. Furthermore, several GaN nanoindentation experiments published in various papers are simulated and briefly discussed.

1.2 Literature Overview

In this section, a brief overview of literature related to the topic of this thesis is given. Some of the more important articles are described in more detail in later chapters.

Background literature on crystal plasticity and the underlying mechanisms can be found in several standard works. Kittel [17] and Hertzberg [7] are hereby the most important reference books in the course of this work.

The mechanical properties of GaN are still subject of discussion, hence, several sources are to be analyzed. In terms of the elastic moduli Nakamura et al. [20] have presented a broad selection of experimental and calculated elastic coefficients alongside their own results, which have been obtained by resonant ultrasound spectroscopy. The Brillouin scattering investigation results by Polian et al. [23] are frequently cited and are important references for this thesis. In the course of the analysis the results of Schwarz et al. [26], which are likewise acquired through resonant ultrasound spectroscopy, have proven to be relevant.

The elastic behavior of Silicon has been studied in more detail compared to GaN and the influence of the orientation of the single crystal structure is explained in detail by Hopcroft et al. [10]. The elastic coefficients of $\langle 111 \rangle$ Silicon have been presented by Kim et al. [16] which also state that $\langle 111 \rangle$ Silicon has preferable mechanical characteristics for micro-electro-mechanical systems compared to the $\langle 100 \rangle$ orientation.

Exact information on the plasticity of GaN is fairly sparse. Relevant studies on this topic have been conducted by Caldas et al. [2] and Wheeler et al. [30] and are discussed later on more in-depth. Most of the necessary information on the crystallographic properties of GaN, such as atomic spacing and slip systems are presented in these papers.

Nanoindentation tests of GaN layers have been conducted by several groups. Results on this topic have been presented by Yu et al. [31] as early as 1999. In this paper Berkovich and spherical indenters are used to examine elastic properties and the hardness of GaN on a sapphire layer. Likewise experiments of GaN on sapphire have also been done by Tsai et al. [27]. Since the substrate inevitably effects the results Nowak et al. [21] have used a bulk crystal to examine the elastic and plastic properties of GaN. Atomic force microscopy images of the indentation are shown by Kucheyev

et al. [18] which illustrate plastic deformation along certain slip planes. Another observation has been the appearance of pop-in events, which indicate the onset of plastic deformation by a sudden increase of indentation depth at constant load.

Such pop-in events have also been reported by Wei et al. [29]. In this study, the differently orientated nonpolar GaN thick films have been examined with a Berkovich indenter. An in-depth analysis of a conical indentation has been done by Huang et al. [11]. Their findings support previously reported assumptions that the plastic deformation of GaN is primarily due to slip in the basal and in pyramidal planes.

1.3   Nanoindentation

Nanoindentation is an important tool to obtain mechanical data of semiconductor materials and it is the experiment modeled by means of FEM within this thesis. Therefore this section is dedicated to explain the concept and the results of the technique as it is demonstrated by Hay [6].

Instrumented indentation testing (IIT) is similar to conventional hardness tests, with the difference that not only the residual deformation caused by an applied force is measured, rather is the instrument able to record the force and the penetration for the entire time that the indenter is in contact with the material.

This is the main advantage of IIT because it theoretically provides enough information to calculate not only the hardness but also additional material parameters, the most important of these is the Young's modulus.

Figure 1.1 (a) shows a schematic representation of the nanoindentation. The indenter is pressed into the probe and leaves a mark behind. The typical test chronology can be split into five test segments. The first one is that the indenter approaches the surface until contact is sensed. Then the indenter is pressed into the material until the maximum force or penetration is reached. The indenter is held for a dwell time at maximum force. In the next segment the indenter is withdrawn from the sample

at a rate similar to the indentation rate until the reaction force is zero. At last it is removed completely from the sample.

For certain experiments, a dwell step during the release can be used to determine the thermal drift of the test material and equipment. In the first evaluation step load-penetration and load-time curves are generated from the obtained data similar to the exemplary ones shown in Figure 1.1 (b) and (c). In the second stage of analysis, material properties are calculated from the data of the load-penetration curve. The calculation, which leads to the Young's modulus, can be found in [6].

In [6], some Young's moduli measured by IIT are shown, which have a quite good agreement with the ones obtained by tensile test, ultrasound, or dynamic mechanical analysis. However, all of the presented values are for polycrystalline or amorphous materials which are more or less isotropic. Single crystal GaN is anisotropic, and, a Young's modulus of GaN calculated this way should be approached with caution. More advanced evaluations for anisotropic materials are given by e.g. [28].
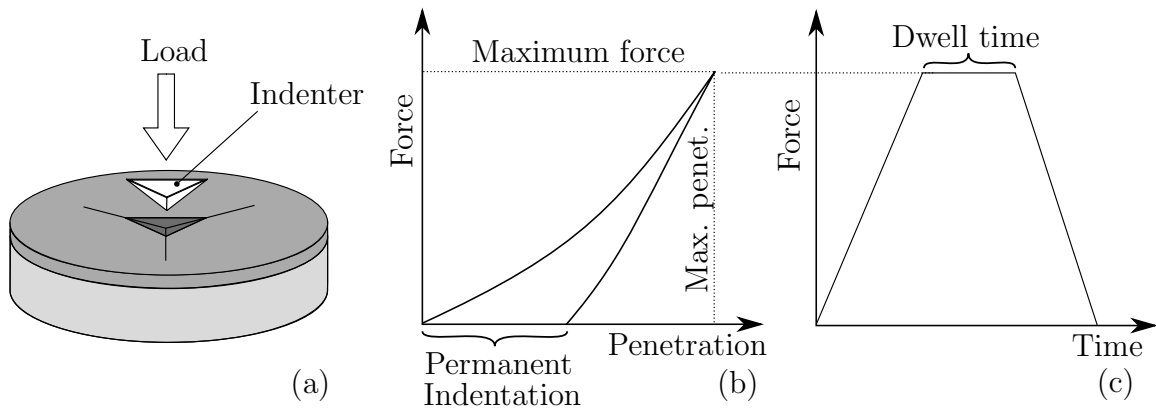
Figure 1.1: Schematic representation of a nanoindentation with a Berkovich indenter (a) and the resulting load-penetration (b) and load-time curves (c).

1.4 KAI Experimental Data

Most of the FEM analyses in this thesis are simulations of the experiments done at the KAI. The structure of the wafer for these experiments is similar to the one described in the work of Reisinger et al. [24] and shown in Figure 1.2 (a). The thin film on the Silicon substrate does not consist of pure GaN. Instead, there are several transition sublayers that reduce the lattice mismatch between GaN and Silicon. Even with these transition layers, there are significant residual stresses in the wafer, which have been characterized in [24] by using ion beam layer removal of a cantilever beam in combination with the ensuing changes of the cantilever bending. The results are shown in Figure 1.2 (b).

The nanoindentation experiments have been done with two different indenters, a Berkovich indenter and a cono-spherical indenter with a tip radius of $2\,\mu m$. For both indenters experiments with three different indentation depths have been carried out.

(a)   (b)
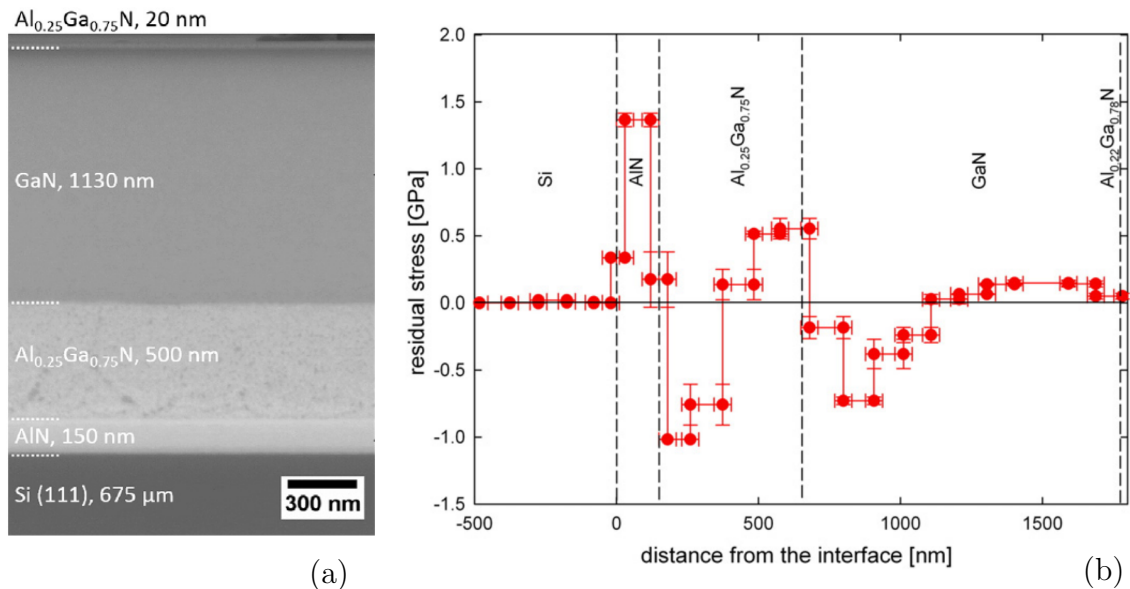
Figure 1.2: The multilayered stack structure on top of the silicone substrate is presented in (a). The bi-axial residual stress distribution in the stack is shown in (b). [24]

Each experiment has been repeated 12 times. The results of four of the six different test are shown in Figure 1.3.

In Figure 1.3 (a) the results of rather small indentations with a Berkovich indenter are shown. At such small indentation depths, even the smallest impurities and crystal defects lead to quite large variations in the load-penetration curves. Another possible source of inaccuracies is the precision of the testing equipment. Nevertheless, a pop-in event around 0.02 μm can be seen for all curves. The results of an indentation with a higher maximum force can be seen in Figure 1.3 (b). The maximum force hereby is 35 mN, which results in a displacement of 0.365 μm. Plot 1.3 (c) shows a similar indentation depth as Figure 1.3 (a) but with a cono-spherical indenter. Here noteworthy is that no plastic deformation takes place. In Figure 1.3 (d) an indentation with the same maximum force as in (b) is shown but in contrast to (b) the cono-spherical indenter is used. Because, the contact area is much bigger in this case, the penetration is smaller at the maximum force. A pop-in event is visible which occurs at around ten times the indentation force and six times the penetration
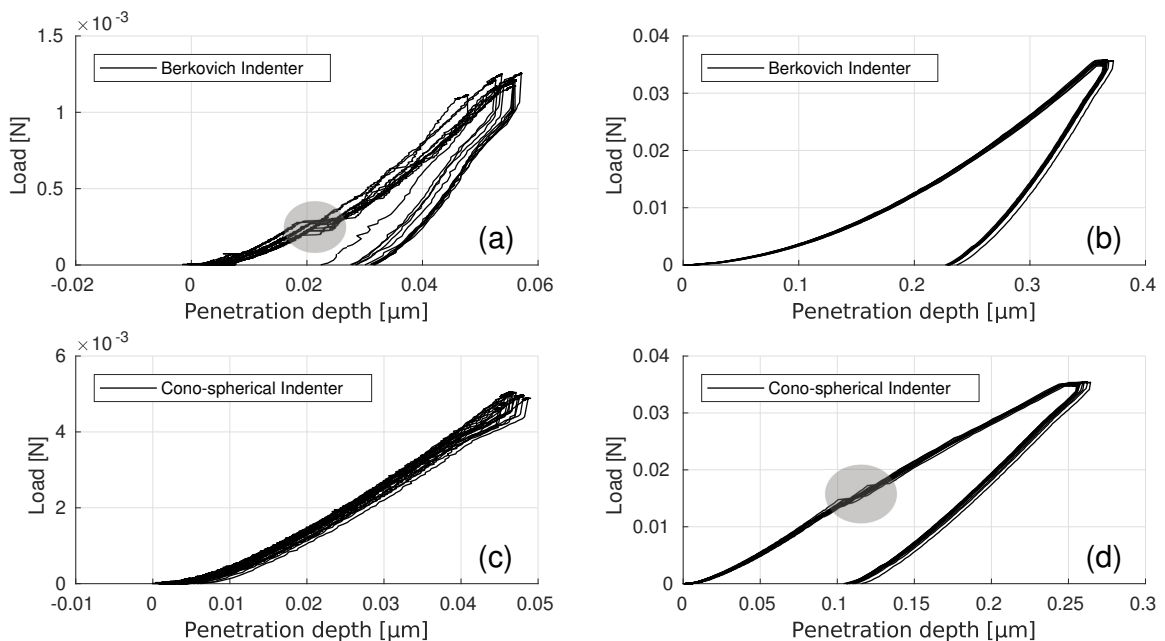
Figure 1.3: Experimental nanoindentation results, a courtesy of KAI GmbH, Villach, done on the wafer described in [24].

depth compared to the one in Figure 1.3 (a). The results of Figure 1.3 (b) are chosen as the main objective for the FEM analysis, because the effects of a late and strong pop-in event as in (d) can not be modeled with the means of this thesis and a smaller indentation depth as in (a) also provides a less reliable result for a simulation.

Chapter 2

Mechanical Properties of Gallium Nitride

One important aspect of this thesis is to find and use elastic and plastic material properties suitable to describe the material response of the tested GaN-on-Silicon Wafer. The influence of the elastic properties of Silicon and GaN are important for the analysis, but the main focus of the theoretical research lies in the modeling of GaN's plastic properties.

To avoid the modeling and computational effort connected with classic crystal plasticity modeling, Hill's plasticity theory is chosen to model the plastic behavior. To be able to apply this criterion correctly, knowledge about the direction dependency of the material properties is required. Therefore, it is necessary to take a closer look at the structure of GaN in order to better understand the mechanical properties and the underlying crystallographic mechanisms responsible for the plastic deformation, and consequently the shape of the nanoindentation curve and the dissipated energy.

2.1 Wurtzit Structure

The crystal structure can be defined as the infinite repetition of identical groups of atoms in an ideal crystal. Such groups are called unit cells or primitive cells. They are attached to further cells throughout a set of mathematical points called the lattice [17]. Many common materials are polycrystalline, which means that the solid does not have the same lattice orientation in the whole body, instead it consists of many different grains of varying size and orientation. In contrast, GaN shares, to some extend, the same lattice orientation over the wafer.

GaN has a Wurtzite crystal structure which belongs to the group of the hexagonal crystal systems. The Wurtzite crystal structure always consists of two compounds, in case of GaN theses are Gallium and Nitrogen. Each of the two compounds is arranged in a separate hexagonal close-packed sublattice.

The lattice constants for the hexagonal structure of GaN are: $a = 3.186$ Å and $c = 5.186$ Å (see Figure 2.1), which is very close to the ideal hexagonal close-packed
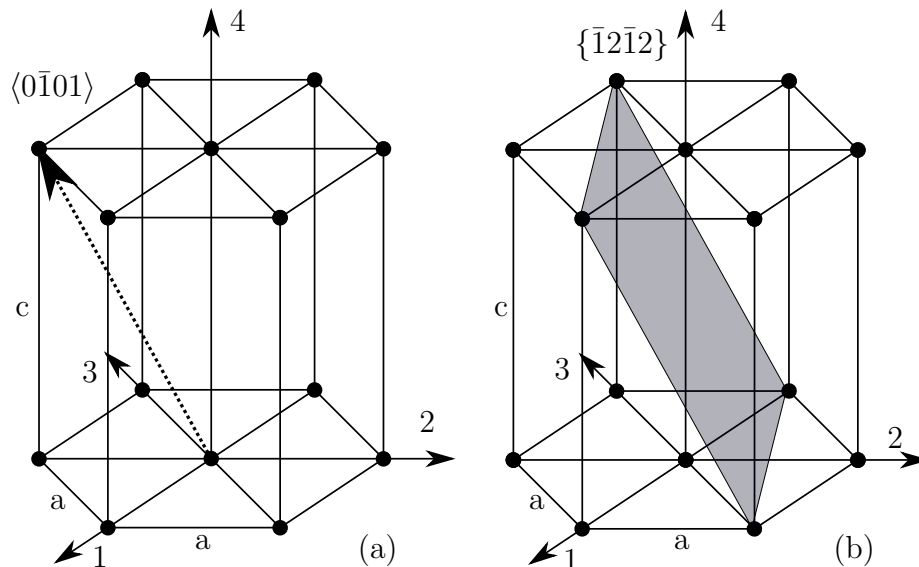
Figure 2.1: Exemplary representation of the Miller-Bravis indices. A crystallographic directions vector is shown in (a) and a crystallographic plane in (b).

structure, that has the ratio $c/a = 1.633$, as stated in [17]. The subsequently used notation to describe crystallographic directions and planes in the hexagonal structure is the Miller-Bravais index. Planes are defined with braces $\{0001\}$ and directions with chevrons $\langle 0001 \rangle$ as shown in Figure 2.1.

Crystallographic directions start in the origin and the indices can be understood as direction vectors as is shown in Figure 2.1(a). In the case of the crystallographic planes, the Miller-Bravis indices describe the intersections with the axes of the coordinate system as demonstrated in Figure 2.1(b).

2.2 Elastic Properties of GaN

Different elasticity values for GaN are examined. In Reichel's thesis isotropic elastic material behavior of GaN is assumed with a Young's modulus of $280\,\mathrm{GPa}$, which was obtained through nanoindentation as described in Section 1.3. Such an isotropic material model might be suitable for a first approximation but looking at the hexagonal crystal structure and keeping in mind that the GaN layers of a wafer form almost a single crystal structure, it follows that an anisotropic elastic formulation would be a better approximation.

Many experimentally obtained or theoretically calculated elasticity values can be found in the literature, which partially deviate strongly. Two experimentally obtained sets of elastic constants reported in the literature will be discussed next.

Schwarz et al. [26] have used a resonance ultrasound spectroscopy method to measure the elastic constants. Their test sample has been a $d_1 = 2.01$ mm, $d_2 = 2.309$ mm, and $d_3 = 0.285$ mm rectangular cuboid probe of bulk GaN. Resonance frequencies have been measured and compared to calculated ones. The calculated frequencies depend on the sample dimension, density, and the elastic constants. Therefore beginning with a first set of approximated elastic constants a fitting procedure has been used to

Table 2.1: Elastic parameters of GaN [GPa] as used for Voigt notation, see Equation (2.1).

Source paper	C_{11}	C_{12}	C_{13}	C_{33}	C_{44}
Schwarz and Khachaturyan [26]	377	160	114	209	81.4
Polian et al. [23]	390	145	106	398	105

achieve a minimum difference between the calculated frequencies and the measured ones by varying the elastic constants.

Polian et al. [23] used a Brillouin scattering investigation to measure the elastic constants of GaN. In such an experiment the anisotropic elastic parameters are calculated through the different sound velocities in the different directions. These are measured by the frequency shift of scattered photons. The values obtained with this procedure are shown in Table 2.1 together with the values from Schwarz et al. [26].

GaNs elastic behavior is transversely isotropic, which means that the elasticity matrix in the 2-index Voigt notation reads

$$\underline{\underline{C}} = \begin{pmatrix} C_{11} & C_{12} & C_{13} & 0 & 0 & 0 \\ C_{12} & C_{11} & C_{13} & 0 & 0 & 0 \\ C_{13} & C_{13} & C_{33} & 0 & 0 & 0 \\ 0 & 0 & 0 & C_{44} & 0 & 0 \\ 0 & 0 & 0 & 0 & C_{44} & 0 \\ 0 & 0 & 0 & 0 & 0 & (C_{11} - C_{12})/2 \end{pmatrix} . \tag{2.1}$$

Inverting the elasticity matrix results in the compliance matrix

$$\underline{\underline{C}}^{-1} = \underline{\underline{S}} = \begin{pmatrix} \dfrac{1}{E_x} & -\dfrac{\nu_{xy}}{E_x} & -\dfrac{\nu_{zx}}{E_z} & 0 & 0 & 0 \\ -\dfrac{\nu_{xy}}{E_x} & \dfrac{1}{E_x} & -\dfrac{\nu_{zx}}{E_z} & 0 & 0 & 0 \\ -\dfrac{\nu_{xz}}{E_x} & -\dfrac{\nu_{xz}}{E_x} & \dfrac{1}{E_z} & 0 & 0 & 0 \\ 0 & 0 & 0 & \dfrac{1}{G_{zx}} & 0 & 0 \\ 0 & 0 & 0 & 0 & \dfrac{1}{G_{zx}} & 0 \\ 0 & 0 & 0 & 0 & 0 & \dfrac{1}{G_{xy}} \end{pmatrix} \quad , \tag{2.2}$$

here, given in terms of the Young's moduli E_i, the Possion's ratio ν_{ij} and the shear moduli G_{ij}. Since the compliance matrix is symmetric the equivalence

$$-\frac{\nu_{xz}}{E_x} = -\frac{\nu_{zx}}{E_z} \tag{2.3}$$

applies.

2.3 Plastic Properties of Single-Crystal GaN

2.3.1 Critical Shear Stress

The elastic properties are only the first part of the material model of Gallium Nitride. Responsible for the typical differences between the loading and the release curve in a nanoindentation experiment is not the elastic behavior, rather it is plasticity which causes the energy dissipation.

A major contribution in the field of crystal plasticity has been the work of Schmid and Boas [25], who have recognized that the yield stress of a single crystal depends strongly on its lattice orientation in regard to the load case.

An isotropic yield criterion as well as an isotropic elastic behavior are therefore only correct for many common materials, because the grain orientations are random. Even

if the individual grains are anisotropic, the overall material behavior is isotropic because the differences of the individual grains tend to average out. In case of a single crystal structure, the crystal orientation cannot be disregarded.

This anisotropic behavior is explained by looking at the main mechanism behind crystal plasticity, i.e. the dislocation motion or glide through the crystal lattice. This dislocation motions occur on certain crystallographic planes in certain crystallographic directions, the so-called slip systems. The glide initiates when the resolved shear stress of the slip system reaches the critical shear stress as shown in Figure 2.2 (a) and (b). The relation between the resolved shear stress τ^{rss} and the corresponding stress state is described by the so-called Schmid's law [25],

$$\tau^{\mathrm{rss}} = \sigma \cos(\lambda) \cos(\phi) \qquad , \tag{2.4}$$
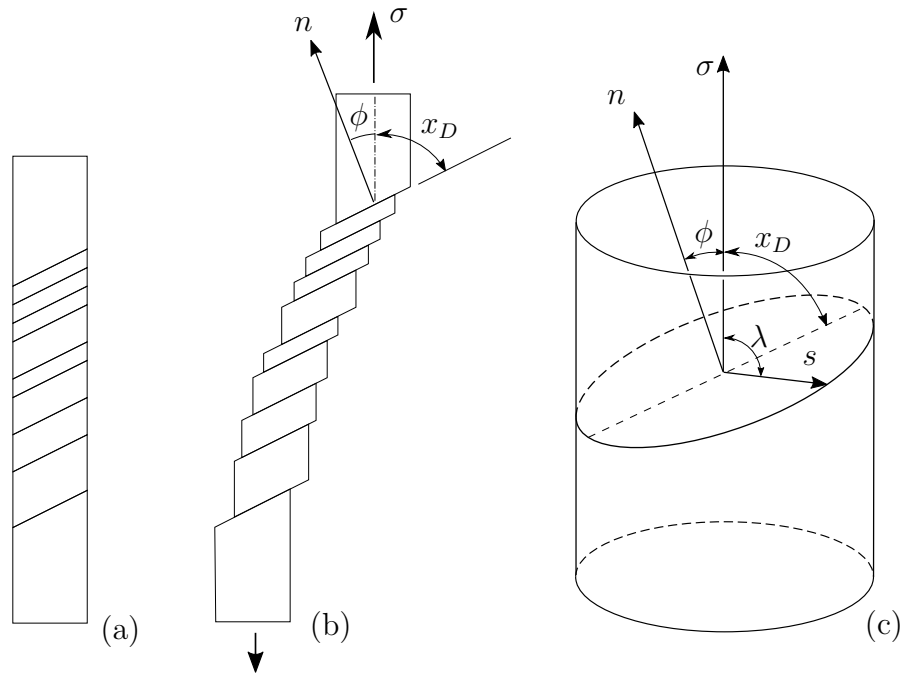
Figure 2.2: Schematic illustration of slip under uniaxial tension in a single crystal (a)(b). Figure (c) shows the angles and directions necessary to calculate the Schmid factor. [7]

where σ is the applied uniaxial stress, λ is the angle between the stress direction and the slip direction s, and ϕ is the angle between slip plane normal n and the uniaxial stress direction (Figure 2.2 (c)). The factor

$$m = \cos(\lambda)\cos(\phi) \tag{2.5}$$

is known as the Schmid factor and ranges from 0 to 0.5. A slip system is activated when the resolved shear stress τ^{rss} reaches the critical value

$$\tau^{\mathrm{crss}} = \sigma^{\mathrm{Y}} \cdot m \qquad , \tag{2.6}$$

and the crystal starts yielding. The uniaxial stress σ is then equal the uniaxial yield stress σ^{Y}. The critical resolved shear stress is therefore a slip system property that can be obtained through experiments, in which the crystal orientation as well as the stress state is known and the activation of the first slip system is observed. Carrying out such experiments is challenging since is difficult to achieve a reliable uniaxial stress state and to take pictures of a slip initiation event.

For each slip system there are stress states where the Schmid factor $m = 0$ and therefore the resolved shear stress is zero. This is the case if the stress state is uniaxial one in slip direction or perpendicular to the slip plane.

Experiments are not the only approach to define the critical shear stresses of a crystal. The so-called Peierls-Nabarro shear stress $\tau^{\mathrm{c}}_{\mathrm{PN}}$ is not obtained empirically instead it is a theoretical calculation of the shear stress required to move a dislocation through a crystal lattice in a particular direction (Hertzberg [7]). It depends on material properties such as the shear modulus and the spacing of atomic planes between which dislocations can glide. Therefore the Peierls-Nabarro stress is a theoretical value and studies (e.g. with copper, nickel, and iron [7]) have shown that it differs from experimental values. Nevertheless, in lack of experimental data, this values can give a first approximation of the critical shear stress of the individual slip systems.

Slip Systems in GaN

In the hexagonal Wurtzite structure of GaN, there are in total eleven slip systems. The six different slip planes in which slip occurs are shown in Figure 2.3. The first one is the $\{0001\}$ or basal plane, then there are the two prismatic planes $\{\bar{1}2\bar{1}0\}$ and $\{1\bar{1}00\}$. The three remaining planes are the pyramidal ones $\{1\bar{1}01\}$, $\{11\bar{2}2\}$, and $\{1\bar{1}02\}$.

All of this slip planes, except the basal one, occur six times in a single crystal cell with a 60° angle around the 4-axis between each iteration. The basal plane is also the only one, which has three equivalent slip directions (i.e. in the $\langle 1000 \rangle$, $\langle 0100 \rangle$ and $\langle 0010 \rangle$ direction) with the same critical shear stress. All other slip planes have two slip directions, which have different critical shear stresses and are therefore, in contrast to the three different slip directions of the basal plane, defined as individual slip systems. In the case of four of the slip planes ($\{\bar{1}2\bar{1}0\}$, $\{1\bar{1}00\}$, $\{11\bar{2}2\}$, and $\{1\bar{1}02\}$), the two slip directions are orthogonal to each other. For example the $\{1\bar{1}00\}$ plane has the $\langle 0001 \rangle$ and $\langle \bar{1}2\bar{1}0 \rangle$ slip directions. Only in case of the $\{1\bar{1}01\}\langle 11\bar{2}3 \rangle$ slip system there are two different possible orientations of the slip direction for each possible orientation
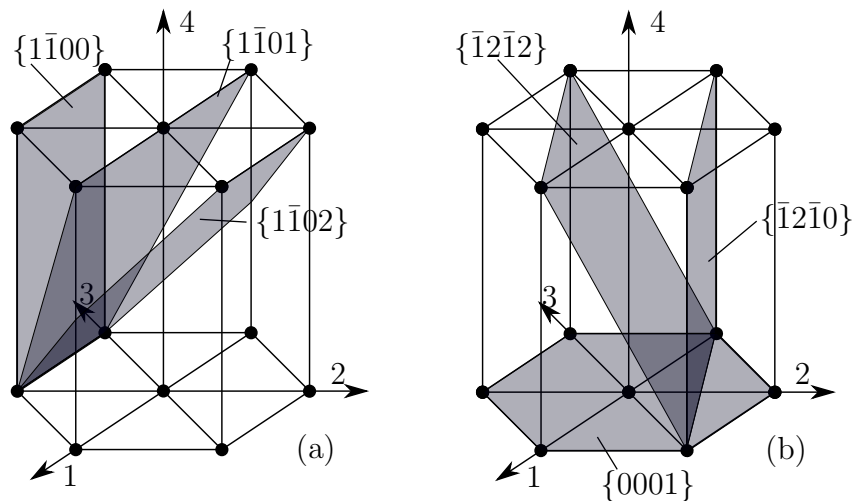
Figure 2.3: The six different slip planes in GaN with the their corresponding Miller-Bravis indices

of the slip plane. They are offset by each other by 31.46° and are not orthogonal to the slip direction of the second slip system of this slip plane. A complete list of all of the slip systems can be found in Appendix A Table A.2

The more and the better information one can get about the critical shear stress of these slip systems the better an elasto-plastic FEM simulation can be. The problem with GaN is that there is not much information available about its plastic properties. The main research focus is on the electrical properties of GaN, since the mechanical properties play, except in the production process, only a minor role for its usage as semiconductor. Moreover, due to its brittle nature, it is very difficult to obtain information like the yield onset under certain load cases. In the following, two papers are presented which have investigated this topic despite these difficulties.

2.3.2 Papers on the Topic of GaN Plasticity

The first important paper on the topic of GaN plasticity is by Wheeler et al. [30]. They have presented experimental plasticity parameters of GaN which have been obtained by in situ micro-compression tests. They have been able to acquire the yield stress of GaN in $\langle 0001 \rangle$ direction and detect the primary slip system $\{11\bar{2}2\}$ $\langle 11\bar{2}3 \rangle$.

The test prisms have been grown on a sapphire substrate and have been doped with silicon with a ratio of Ga:Si = 12050:1. The compressions have been performed with a Zeiss DSM 962 SEM with an Alemnis in Situ Indenter, whereas a minimum of six prisms have been tested in each test series.

A broad selection of different data has been collected, being the yield stress at room temperature the most important information for this thesis. Furthermore, the temperature dependency, as well as the strain rate sensitivity, have been studied.

The yield stress has been measured to be 7.85 GPa at 24.5 °C under uniaxial stress in the $\langle 0001 \rangle$ direction. Figure 2.4 shows stress-strain data from a micro-compression

strain rate jump test with different strain rates through the compression. The influence of the strain rate is also shown in the Figure. It is amibigous that the elastic modulus in all of the tests has been around 100 GPa. This is much lower then the values given in [26] and [23] or the isotropic values which have been used by Reichel. An angle of 48° has been observed between the slip plane and the compression axis and it has been therefore assumed, in consideration of the calculated Schmid factors that the main slip system is the $\{11\bar{2}2\}$ $\langle11\bar{2}3\rangle$ one.

It has to be mentioned that the Schmid factors and the direction angles presented in [30] deviate from the ones stated in [2] and the ones calculated in the course of this thesis. Therefore their assumption of the main slip system should be considered with caution.

Caldas et al. [2] have studied nanoscale plasticity of GaN, through nanoindentation with a very small cono-spherical indenter. A 4 μm thick GaN film grown on c-plane sapphire substrate has been indented with a Hysitron TriboScope nanoindenter. The indentations have been performed using a cono-spherical tip "with a radius of curva-
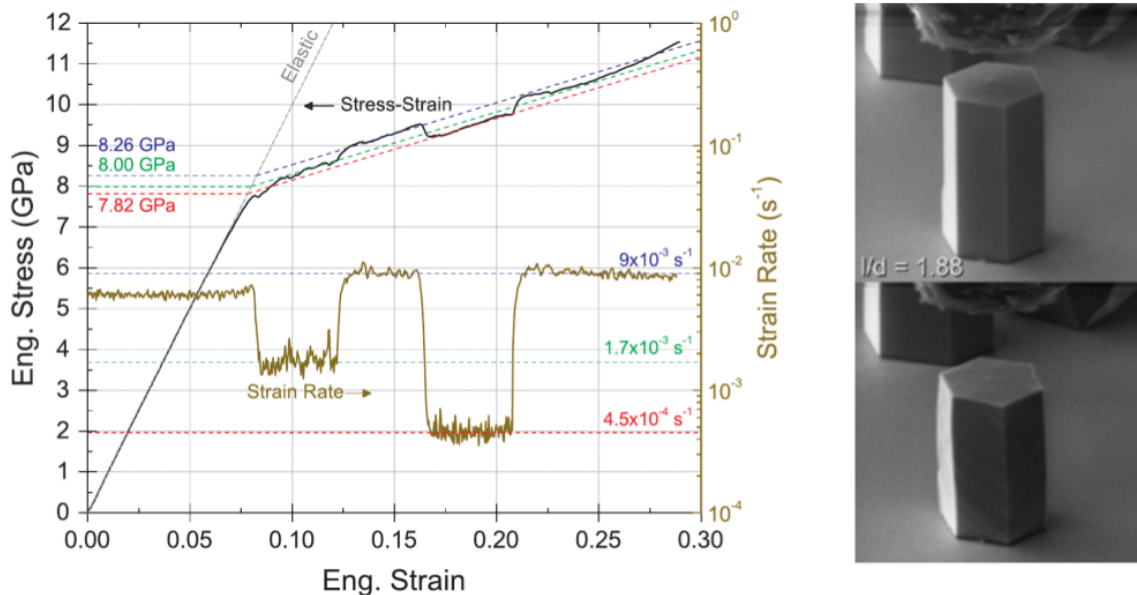
Figure 2.4: Strain stress curve from [30]. The picture on the right is also taken from [30] and shows the deformation of a GaN pillar. The aspect ratio of this probe is 1.88 (height to diameter).

ture of ~260 nm and ~90 nm in height" [2]. Additionally to load-penetration curves, transmission electron microscopy (TEM) and atomic force microscopy (AFM) pictures of the indentation have been made, which give a good impression of the active slip systems. Figure 2.5 (a) is taken with a two-beam diffraction condition $\mathbf{g} = \langle 0002 \rangle$, (b) with $\mathbf{g} = \langle 1\bar{1}00 \rangle$. Especially in Figure 2.5 (b) the plastic deformation in direction of the slip planes is well visible. Directly beneath the indentation dislocations on the pyramidal planes are visible. To the side of the indentation slip on the basal planes occurs. Moreover, the begin of plastic deformation has been observed to occur in connection with a pop-in event. The pop-in event is a sudden increase in penetration depth with no variation of the applied force. These pop-in events appear at an indentation depth of approximately 40nm, with no residual indentation remaining at lower indentation depths.

The calculated Peierls-Nabarro stresses are another important information that can be used to model GaN plasticity. The values taken from the paper [30] are presented in Table 2.2. Supported by the TEM pictures and Peiers-Nabarro critical shear stresses the authors claim that slip directly beneath the indentation tip occurs after the first pop-in event preferentially along the $\{1\bar{1}01\}\langle11\bar{2}3\rangle$ and $\{11\bar{2}2\}\langle11\bar{2}3\rangle$ slip systems. Additionally, the basal $\{0001\}\langle\bar{1}2\bar{1}0\rangle$ slip system gets activated at the edge of the indent.
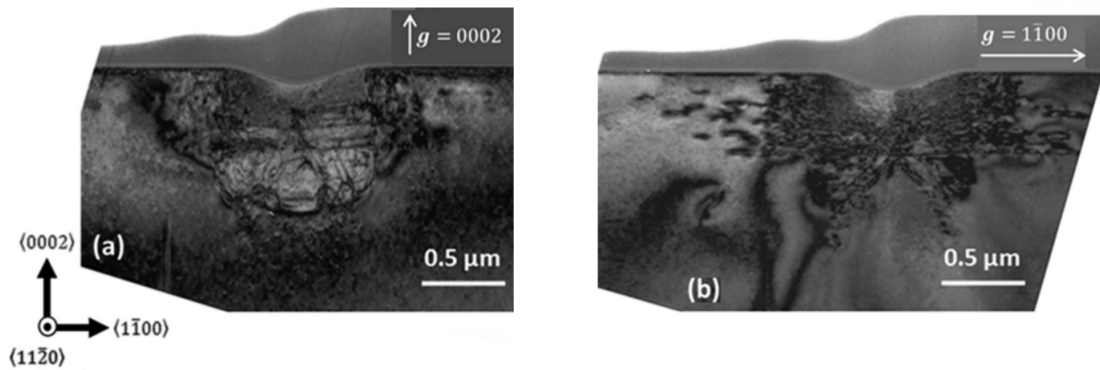
Figure 2.5: Bright-field TEM pictures of an indent in the GaN layer showing dislocations in various slip systems. [2]

Table 2.2: Slip systems, the Schmid factors m for a load perpendicular to the basal plane, and the Peierls-Nabarro stresses $\tau_{\mathrm{PN}}^{\mathrm{c}}$ [30].

Slip system		m	$\tau_{\mathrm{PN}}^{\mathrm{c}}$ [GPa]
$\{0001\}$	$\langle\bar{1}2\bar{1}0\rangle$	0	2.34
$\{\bar{1}2\bar{1}0\}$	$\langle0001\rangle$	0	16.5
	$\langle1\bar{1}00\rangle$	0	19.7
$\{1\bar{1}00\}$	$\langle0001\rangle$	0	10.4
	$\langle\bar{1}2\bar{1}0\rangle$	0	1.21
$\{1\bar{1}01\}$	$\langle11\bar{2}3\rangle$	0.40	54.7
	$\langle\bar{1}2\bar{1}0\rangle$	0	11.3
$\{11\bar{2}2\}$	$\langle11\bar{2}3\rangle$	0.45	29.8
	$\langle1\bar{1}00\rangle$	0	23.3
$\{1\bar{1}02\}$	$\langle1\bar{1}01\rangle$	0.49	85.3
	$\langle\bar{1}2\bar{1}0\rangle$	0	15.2

2.4 Hill's Potential

To predict plastic deformations (e.g. in an FEM simulation) three rules have to be provided [3]:

- **Yield criterion**

  The yield criterion f defines whether a stress state leads to a pure elastic system response ($f < 0$) or there is also plastic deformation ($f = 0$). The surface, which is defined by this criterion in the stress space is called yield surface.

- **Flow rule**

  The flow rule provides the connection between the stress state and the plastic strain increment if the yield criterion is fulfilled.

- **Hardening rule**

  In general the yield surface changes throughout the deformation, which is defined by the hardening rule.

The research presented so far has shown that in line with the anisotropic elastic behavior an anisotropic plastic behavior for single crystal GaN has to be assumed. The greatly differing Peierls-Nabarro stresses and the different active slip planes shown in the TEM pictures are further indications for the need of an anisotropic plasticity material model. On the one hand, a classic crystal plasticity model is ruled out for the present work because of the associated computation effort and the complexity of the sought simulation. On the other hand, a J2 plasticity model would not be able to account for the anisotropic single crystal structure of the material. Therefore, a reasonable compromise is chosen which could comply with the anisotropy and also would not increase the simulation effort too much. Hill's Potential [13] (also called Hill's yield criterion) fulfills both conditions.

Hill's Criterion was originally developed for rolled sheets but can be used for other applications as long as three orthogonal planes of symmetry are preserved [8]. The intersections of these orthogonal planes are called principal axes of orthotropy. The different yield stress for these axes σ_{xx}^{Y}, σ_{yy}^{Y}, and σ_{zz}^{Y} and their corresponding yield shear stresses τ_{xy}^{Y}, τ_{yz}^{Y} and τ_{xz}^{Y} are set in relation to a reference yield stress σ_0 to calculate the yield stress ratios

$$
\begin{aligned}
R_{xx} &= \frac{\sigma_{xx}^{Y}}{\sigma_0} & R_{xy} &= \sqrt{3}\frac{\tau_{xy}^{Y}}{\sigma_0} \\
R_{yy} &= \frac{\sigma_{yy}^{Y}}{\sigma_0} & R_{yz} &= \sqrt{3}\frac{\tau_{yz}^{Y}}{\sigma_0} \\
R_{zz} &= \frac{\sigma_{zz}^{Y}}{\sigma_0} & R_{xz} &= \sqrt{3}\frac{\tau_{xz}^{Y}}{\sigma_0}
\end{aligned}
\qquad , \tag{2.7}
$$

which are subsequently used for the calculation of six Hill constants as,

$$
\begin{aligned}
F &= \frac{1}{2}\left(-\frac{1}{R_{xx}^2} + \frac{1}{R_{yy}^2} + \frac{1}{R_{zz}^2}\right) & L &= \frac{3}{2}\left(\frac{1}{R_{yz}^2}\right) \\
G &= \frac{1}{2}\left(\frac{1}{R_{xx}^2} - \frac{1}{R_{yy}^2} + \frac{1}{R_{zz}^2}\right) & M &= \frac{3}{2}\left(\frac{1}{R_{xz}^2}\right) \\
H &= \frac{1}{2}\left(\frac{1}{R_{xx}^2} + \frac{1}{R_{yy}^2} - \frac{1}{R_{zz}^2}\right) & N &= \frac{3}{2}\left(\frac{1}{R_{xy}^2}\right)
\end{aligned}
\qquad . \tag{2.8}
$$

These Hill constants are used in an extension of the von Mises criterion. Therefore the equivalent stress is given as

$$
\sigma_{\text{equ}} = \sqrt{F(\sigma_{yy} - \sigma_{zz})^2 + G(\sigma_{zz} - \sigma_{xx})^2 + H(\sigma_{xx} - \sigma_{yy})^2 + 2L\tau_{yz}^2 + 2M\tau_{xz}^2 + 2N\tau_{xy}^2} \; . \tag{2.9}
$$

The yield function of the Hill's criterion can than be written as

$$
f = \sigma_{\text{equ}} - \sigma_0 \qquad , \tag{2.10}
$$

whereas σ_0 is the current reference yield stress, which increases if Equation (2.10) is fulfilled and the material deforms plastically. The plastic strain-increment relations written in the same 2-index Voigt notion of Equation (2.2) are then defined as

$$
\begin{pmatrix} d\epsilon_{xx}^{\text{pl}} \\ d\epsilon_{yy}^{\text{pl}} \\ d\epsilon_{zz}^{\text{pl}} \\ d\gamma_{yz}^{\text{pl}} \\ d\gamma_{xz}^{\text{pl}} \\ d\gamma_{xy}^{\text{pl}} \end{pmatrix} = \frac{d\lambda}{\sigma_{\text{equ}}} \begin{pmatrix} H(\sigma_{xx} - \sigma_{yy}) - G(\sigma_{zz} - \sigma_{xx}) \\ -H(\sigma_{xx} - \sigma_{yy}) + F(\sigma_{yy} - \sigma_{zz}) \\ -F(\sigma_{yy} - \sigma_{zz}) - G(\sigma_{zz} - \sigma_{xx}) \\ 2L\tau_{yz} \\ 2M\tau_{xz} \\ 2N\tau_{xy} \end{pmatrix} \quad , \tag{2.11}
$$

where λ is the plastic multiplier. The hardening law has to be defined separately.

2.4.1 Transverse Isotropy in the Hill Yield Criterion

In the original publication of Hill's plasticity theory [8], Hill has presented a way to reduce the orthotropic yield criterion to a transversely isotropic one. Although GaN has three symmetry planes perpendicular to the basal plane and is therefore not transversely isotropic, this formulation of the yield criterion is interesting for this study because it reduces the number of required yield stresses. Moreover, it is not really possible to comply with GaNs radial direction dependency since the exact material orientation of the experimentally tested wafers is not known and GaN has other symmetry planes than an orthotropic material behavior.

If one presumes that there is a rotational symmetry about the z-axis, rewrites equation (2.9) as

$$
\begin{aligned}
\sigma_{\text{equ}}^2 = [(G+H)\sigma_{xx}^2 - H\sigma_{xx}\sigma_{yy} + (F+G)\sigma_{yy}^2 + 2N\tau_{xy}^2] - \\
-2(G\sigma_{xx} + F\sigma_{yy})\sigma_{zz} + 2(L\tau_{yz}^2 + M\tau_{xz}^2) + (F+G)\sigma_{zz}^2 \quad ,
\end{aligned}
\tag{2.12}
$$

and performs a coordinate rotation with angle θ around the z-axes, one can draw some insights about the transversely isotropic Hill parameters. Utilizing the equations of transformation and some mathematical connections (for details refer to [8]) the parameters of the Hill yield criterion simplify to

$$
N = F + 2H = G + 2H, \qquad L = M \quad .
\tag{2.13}
$$

This means that the yield stresses σ_{zz}^{Y}, $\sigma_{xx}^{\text{Y}} = \sigma_{yy}^{\text{Y}}$ and $\tau_{xz}^{\text{Y}} = \tau_{yz}^{\text{Y}}$ have to be defined and that the shear yield stress τ_{xy}^{Y} can be calculated through Equation (2.13).

Chapter 3

Modeling Approach for Single Crystal Plasticity

The first part of this chapter is dedicated to explaining how Hill's plasticity theory can be used to model anisotropic single crystal plasticity under consideration of the active slip systems and their critical slip stresses. This is done on the example of Gallium Nitride but this approach can also be applied to other anisotropic single crystal materials. The theoretical background on the plastic behavior of GaN and the transversely isotropic Hill yield criterion is presented in Chapter 2.

In the second part of this chapter, the single element FEM simulations, used to verify the behavior of the modeling approach, are discussed briefly. ANSYS APDL v18.1 (ANSYS Inc., Canonsburg, PA, USA) is employed for the FEM simulations.

3.1   GaN Plasticity

In order to use the Hill yield criterion for GaN, some consideration have to be made. Appropriate values for the three needed yield stresses must be chosen in connection with the values presented in the literature [2, 30].

As described in Section 2.3.2 the uniaxial compression yield stress in $\langle 0001 \rangle$ direction is 7.85 GPa. From here on the $\langle 0001 \rangle$ direction will be identical with the z-axis of the simulation. σ_{zz}^{Y} is defined to be equal to the reference yield stress σ_0, hence the Hill parameter $R_{zz} = 1$.

Since there is no available experimental data for $\sigma_{xx}^{\mathrm{Y}} = \sigma_{yy}^{\mathrm{Y}}$ and $\tau_{xz}^{\mathrm{Y}} = \tau_{yz}^{\mathrm{Y}}$ the calculated Peierls-Nabarro stresses presented in Section 2.3.2 are the only available data concerning yielding in these directions. For a uniaxial load perpendicular to the z-axis, slip can occur theoretically in all slip systems, except in the basal plane.

To know the first slip system to become active under such a load, it is necessary to determine the Schmid factors of all of the systems. A straight forward way to do this is to transform the stress state in question to the local coordinate system with the same orientation as the slip system. To be able to conduct such calculations a fixed orientation of the crystal is chosen. The selected orientation is shown in Figure 3.1 (a). This allows the angles between the slip plane and the global coordinate system to be calculated. In the special case of the hexagonal crystal structure, the two slip
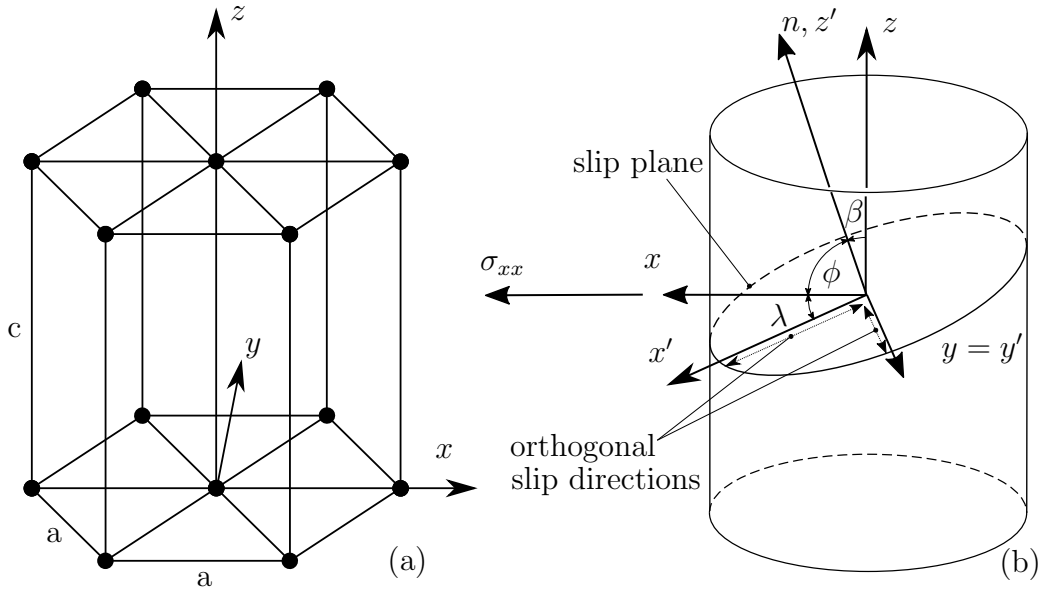
Figure 3.1: Figure (a) shows the chosen global coordinate system definition. Figure (b) shows the local coordinate system of a slip system.

directions of each individual slip systems, with the exception of the basal and the $\{1\bar{1}01\}$ planes, are orthogonal to each other. For these slip systems one can define a local coordinate systems with the x' and the y'-axises orientated in the slip directions.

The resolved shear stresses of the two slip directions of this slip plane are then equal to $\tau_{z'x'}$ and $\tau_{z'y'}$. To calculate the Schmid factor of one slip system one can use a uniaxial stress state equal to 1 defined in the global coordinate system in the direction in question and use the suitable transformation

$$\underline{\underline{R}}\,\underline{\underline{\sigma}}\,\underline{\underline{R}}^{\mathrm{T}} = \begin{pmatrix} \sigma_{x'x'} & \tau_{x'y'} & \tau_{x'z'} \\ & \sigma_{y'y'} & \tau_{y'z'} \\ sym. & & \sigma_{z'z'} \end{pmatrix} \quad , \tag{3.1}$$

to the local coordinate system. The rotation matrix $\underline{\underline{R}}$ is defined for the z-$\tilde{y}$-$\tilde{\tilde{z}}$ Euler angle sequence (refer Appendix A) and must be calculated for each slip system according to the considered orientation. The Schmid factors of the two slip directions are, in the case of the four slip systems with orthogonal slip directions, equal to $\tau_{z'y'}$ and $\tau_{z'x'}$.

In order to facilitate fundamental understanding of this process, the basic concept is explained here using the simple schematic example shown in Figure 3.1 (b). With just one rotation around the y-axis and a uniaxial stress state $\sigma_{xx} = 1$, the calculation takes the form

$$\begin{pmatrix} \cos\beta & 0 & -\sin\beta \\ 0 & 1 & 0 \\ \sin\beta & 0 & \cos\beta \end{pmatrix} \begin{pmatrix} 1 & 0 & 0 \\ 0 & 0 & 0 \\ 0 & 0 & 0 \end{pmatrix} \begin{pmatrix} \cos\beta & 0 & -\sin\beta \\ 0 & 1 & 0 \\ \sin\beta & 0 & \cos\beta \end{pmatrix}^{\mathrm{T}} =$$
$$= \begin{pmatrix} \cos\beta\cos\beta & 0 & \sin\beta\cos\beta \\ 0 & 0 & 0 \\ \sin\beta\cos\beta & 0 & \cos\beta\cos\beta \end{pmatrix} , \tag{3.2}$$

with

$$\tau_{z'x'} = \sin\beta\cos\beta = \cos(90° - \beta)\cos\beta \tag{3.3}$$

and with regard to Figure 3.1, and

$$\beta = \lambda$$
$$90° - \beta = \phi$$

(3.4)

one can see that $\tau_{z'x'} = \cos\phi \cos\lambda = m$ (see Equation (2.4)). For the Schmid factor of the second slip direction applies $\tau_{z'y'} = m = 0$, which is as to be expected since this slip direction is perpendicular to the uniaxial load.

In general six different slip plane orientations around the z-axis have to be considered. For the $\{1\bar{1}01\}$ slip plane the process is even more complicated because the two slip directions are not orthogonal to each other and their Schmid factors have to be considered for each possible slip plane orientation separately. The general calculations for GaN are done in Matlab R2017b (The MathWorks Inc., Natick, MA, USA) and can be comprehend with the in Appendix A displayed information. Also included in Appendix A are the calculated Schmid factors (see Table A.2).

The lowest yield stress for $\sigma_{xx}^{\text{Y}} = \sigma_{yy}^{\text{Y}}$ calculated this way is due to slip in the prismatic $\{1\bar{1}00\}\langle\bar{1}2\bar{1}0\rangle$ system. It is noteworthy that these yield stresses are depended on the coordinate system used for the calculation (see Figure 3.1 (a)). However, this influence is rather small. The yield stress varies for example rotationally around the z-axis between 2.69-2.79 GPa. In this work the higher value of 2.79 GPa is used for the transversely isotropic formulation.

A similar procedure is used to examine the critical value for shear stress τ_{xz}, which is, as to be expected, the shear stress in the basal plane. Together with equation (2.13) all of the needed yield stresses are defined to be

$$\sigma_{zz}^{\mathrm{Y}} = \sigma_0 = 7.85\,\mathrm{GPa}$$
$$\sigma_{xx}^{\mathrm{Y}} = \sigma_{yy}^{\mathrm{Y}} = 2.79\,\mathrm{GPa}$$
$$\tau_{xz}^{\mathrm{Y}} = \tau_{yz}^{\mathrm{Y}} = 2.34\,\mathrm{GPa} \tag{3.5}$$
$$\tau_{xy}^{\mathrm{Y}} = \sqrt{\frac{\sigma_{zz}^2 \sigma_{xx}^2}{4\sigma_{zz}^2 - \sigma_{xx}^2}} = 1.42\,\mathrm{GPa} \qquad .$$

This allows the calculation of the Hill input parameter as

$$R_{zz} = 1$$
$$R_{xx} = R_{yy} = 0.3554$$
$$R_{xz} = R_{yz} = 0.5163 \tag{3.6}$$
$$R_{xy} = 0.3128 \qquad .$$

A constant tangent modulus is used to describe isotropic hardening behavior. It is difficult to make assumptions on the tangent modulus of the GaN since the only information has been the findings of [30]. Therefore tangent moduli of 0, 50, and 100 GPa are evaluated.

3.2   Single Element Simulations

Single element simulations are a crucial tool to evaluate whether or not Hill's yield criterion performs as one expects. Single element simulations use the simplest geometric model that can be created, nevertheless, they are an important tool to understand if nonlinear material models are applied correctly. The main advantage is their simplicity and that their results can, therefore, be comprehended analytically.

To create a single element simulation in ANSYS a linear, fully integrated, 8-node element has to be constrained with the boundary displacement conditions corresponding to the desired load case. The load cases have to be as simple as possible to allow the user to draw conclusions on the plasticity formulation. Therefore uniaxial stress as shown Figure 3.2 (a) and simple shear stress states illustrated in Figure 3.2 (b) are introduced with displacement boundary conditions. Hill's yield criterion is combined with an isotropic elastic material model ($E = 100\,\mathrm{GPa}$ and $\nu = 0.26$) and a constant tangent modulus of 12 GPa. Stress and strain data are then transferred to a Matlab post processing script. To test the Hill yield criterion under certain circumstances a local coordinate system can be used to define the material orientation.

In the beginning, such tests are made to test extreme cases of the Hill parameters and to analyze the resulting stress states and elasto-plastic deformations. After the introduction of the GaN plasticity model, these tests are extended to assess the shear stresses in the slip systems under certain load cases.

The results of one of these single element tests are shown in Figure 3.3, in which (a) illustrates the considered $\{1\bar{1}00\}$ $\langle\bar{1}2\bar{1}0\rangle$ slip system and Figure 3.3 (b) shows the stress-strain data for the local shear stress in the slip system and for the global uniaxial stress state in x-direction.
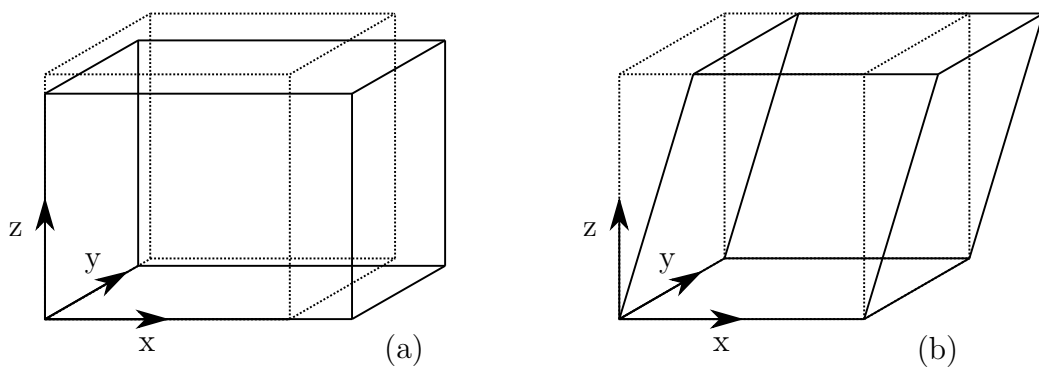
Figure 3.2: Schematic of single element tests. Figure (a) results in a uniaxial σ_{xx} stress state and (b) shows an τ_{xz} stress state.

It is verified that the shear stress in the prismatic system is reached at the yield begin. The critical shear stress of this slip system is 1.21 GPa (Appendix A, Table A.2) and the yield stress in the x-direction is, as explained in Section 3.1, defined to be 2.79 GPa. As to be expected, both values are reached at the same time. A similar result is achieved for the other directions. For instance the yield onset for a simple shear stress $\tau_{xz} = 2.34\,\mathrm{GPa}$ is the same as the critical shear stress of the basal plane.

The single element test also reveals the shortcomings of the material modeling approach. The usage of transverse isotropy has the consequence that a rotation of the material orientation around the z-axis of the coordinate system has no influence on the outcome. In reality there should be small differences in line with the six-folded symmetry of the GaN crystal.

In a theoretical perfect material model plastic behavior should only be initiated if the critical shear stress of a slip system is reached. In case of the presented modeling approach plastic behavior can be initiated even if the critical value has not yet been reached in any slip system. This is due to smeared nature of the approach in which only one overall plasticity criterion is responsible for the yield begin. Furthermore, the
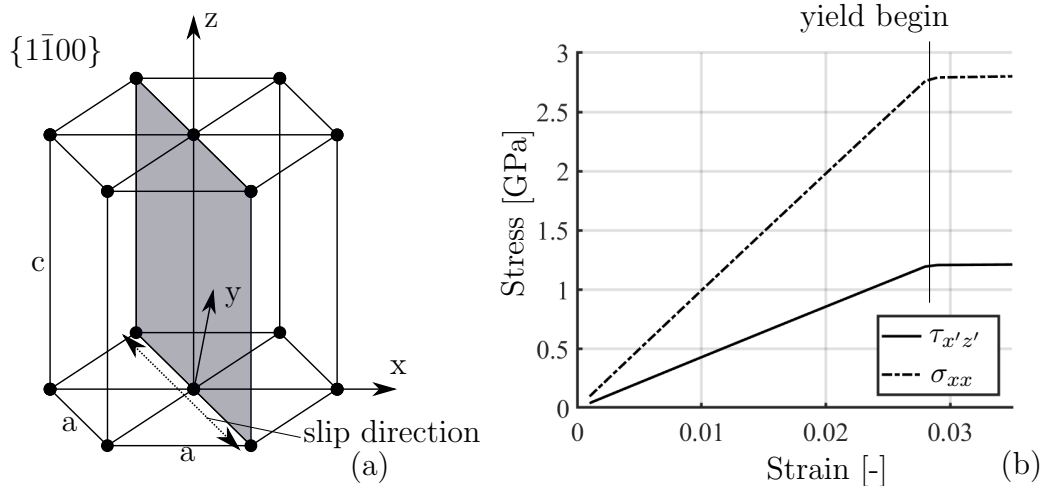
Figure 3.3: Figure (a) illustrates the active slip system. The global strain-stress response due to a uniaxial stress state σ_{xx} is shown as the dashed line in Figure (b) and the shear stress in the local coordinate system of the active slip system is depicted as the solid line.

chosen hardening rule is rather rudimentary and an in-depth analysis and modeling of GaN single crystal plastic deformations by Hill is out of the scope of this thesis, especially considering that not much experimental data on this topic is available.

In summary, it can be said that the approach works well, given the circumstances and boundaries resulting from the usage of the transversely isotropic Hill yield criterion. In the end, the main goal of this approach is to model the overall plasticity, with taking the slip system into account, and without too much computational and handling effort.

Chapter 4

Finite Element Model

The next step after defining and verifying the plasticity approach for GaN is to use it in the simulation of the nanoindentation experiment. Hereby, the used simulation software is again ANSYS. The input scripts for the simulations are written in the ANSYS Parametric Design Language (APDL), which is convenient for testing different model parameters. Two different modeling approaches are used in course of this thesis. To get a basic understanding of the structural response an axisymmetric model is created. For most of the in-depth analysis, a 3D continuum model is used. The significant drawback of the axisymmetric model is that the exact stress state beneath the Berkovich indenter cannot be pictured correctly. Nevertheless, the axisymmetric model is an important step in the development of this project and it can be used for first approximations of the problem.

The first and largest part of this chapter is dedicated to explaining the 3D nanoindentation model. The used material models are summarized and displayed in the following section. How the residual stress states are applied, the features of the axisymmetric model, and a brief verification of the 3D model complete the chapter.

4.1 3D Nanoindentation Model

4.1.1 Geometry

The first step in the creation of a finite element model is to reduce the real problem to an abstract one, which is simple enough to be simulated but at the same time reflects the essential characteristics of the problem. In the case of the nanoindentation experiment, the complex experimental setup is narrowed down to the indenter tip and the required part of the wafer. The geometric shapes of these two parts are defined and then the appropriate boundary conditions, mesh size, element types, and material properties are provided for the simulation.

Geometry of the wafer

The 3D model should be able to represent the real experimental setup without being unnecessarily large. The contact surface of the Berkovich tip is a three-sided pyramid, which has three planes of symmetry. The direction of the load is the same as the main axes of the indenter, therefore the load symmetry is the same as the geometric symmetry of the indenter [19]. According to this considerations, only a sixth of the entire system has to be modeled as shown in Figure 4.1 (a) and (b).
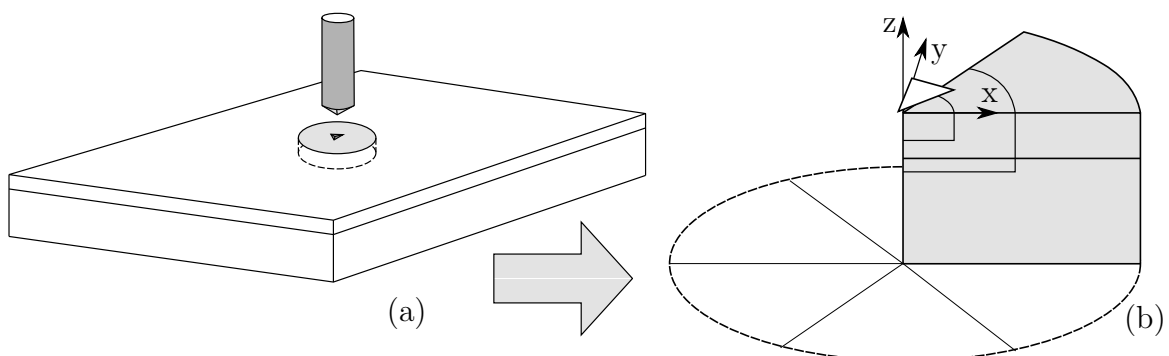
Figure 4.1: Schematic drawing of the experimental setup (a) and the 3D model used for the simulation (b).

The overall size has to be chosen large enough so that the boundary conditions have no influence on the outcome of the indentation regarding stress distribution and load-penetration curve. For the indentation depth of $0.365\,\mu m$, a cross-section with the same height and width equal to $32\,\mu m$ proves to be large enough, so that the boundary condition have no influence on the system response. This quadratic shape is used to create a $60°$ section of a cylinder.

The division in the subparts ensues according to two different characteristics. The distinction between GaN stack and Si substrate is due to the different materials and the different residual stresses. The APDL input script is designed to allow a more in detail analysis of the stack by adding more partitions in the vertical direction. The two subregions, which are visible in Figure 4.1 (b), are added for a better mesh generation and for defining the contact region. The size of these regions is governed by the maximum indentation depth.

In the case of the experiments presented in Section 1.4, Figure 1.3, the stack design is simplified to a homogeneous stack, which has the material model of pure GaN. This is justified because AlN has been reported to behave similarly to GaN.

Shape of the indenter

Since the material of the indenter is much stiffer then the probed GaN, it is assumed that the indenter is rigid. Therefore, only the indenter surface is modeled. The shape of this surface is important because it has a direct and significant influence on the shape of the load-penetration curve and the resulting stress state.

Most of the experiments done by the KAI use a Berkovich tip, which is very commonly used for testing the indentation hardness of a material. A schematic representation is shown in Figure 4.2 (a). The geometry is defined with the so-called half angle $\alpha_b = 65.3°$. All other angles are based on this half angle and the three-fold symmetry of the indenter. A Berkovich tip is in reality imperfect and has a rounding at the

apex of the indenter [6]. This is not modeled in the simulation due to the unknown shape of this imperfection and the expected small influence of it on the solution.

As it is mentioned in the previous section the three-fold symmetry of the indenter determines how big the section of the wafer and the indenter has to be for the 3D model. In line with the geometry model of the wafer, only one sixth of the Berkovich indenter has to be modeled. The cut-out piece of the Berkovich tip in Figure 4.2 (a) matches the geometry modeled in the simulation.

A conical tip as shown in Figure 4.2 (b) is interesting because it can be used as an approximation of a Berkovich indenter in an axisymmetric simulation. Although the exact shape of the Berkovich indenter cannot be considered in an axisymmetric simulation, the same result of the area function can be achieved with the right half angle α_c. The area function describes the contact surface A of the indenter during an experiment [6]. For an ideal Berkovich indenter, the area function is
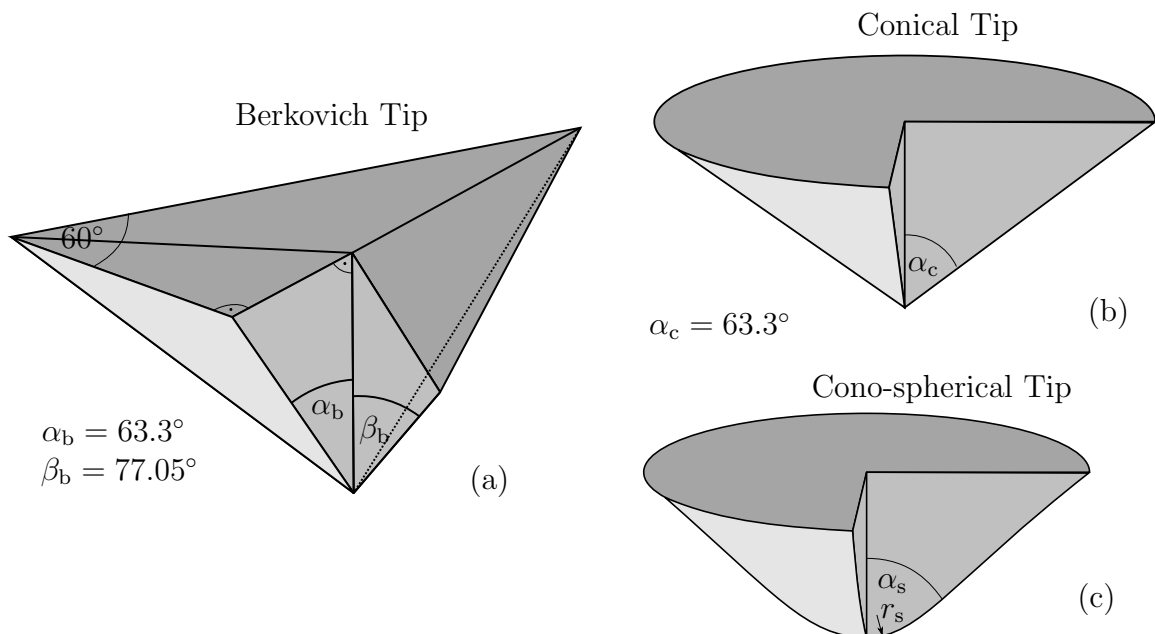
Figure 4.2: Geometric illustration of the three indenter types modeled in this thesis. Figure (a) shows a Berkovich tip, Figure (b) an conical tip which is used to represent a Berkovich tip in an axisymmetric simulation, and Figure (c) shows a cono-spherical tip.

$$A_b = 24.56h_c^2 \tag{4.1}$$

with h_c being the so-called contact depth, which is depended on penetration, the contact stiffness, and contact force. Together with the area function of the conical indenter

$$A_c = \pi \tan^2(\alpha_c)h_c^2 \tag{4.2}$$

one can calculated the equivalent half angle as

$$\alpha_c = \tan^{-1}\sqrt{24.56/\pi} = 70.3°. \tag{4.3}$$

The cono-spherical tip Figure 4.2 (c) is also added to the simulation since results with such an indenter are provided in the literature. It differs from the conical tip by a radius at the apex. This radius can be quite large compared to the indentation depth. In case of cono-spherical indenter experiments conducted at the KAI, it has been $2\,\mu m$ compared to an indentation depth of $0.250\,\mu m$.

4.1.2 Elements and Mesh

The general 3D structure of the wafer consists of 3D continuum elements (SOLID185). These are used in their linear tetrahedral formulation in which case they are defined by four nodes having three degrees of freedom at each node. They are fully integrated and use a pure displacement formulation. For certain analyses, quadratic 10-node tetrahedral continuum elements (SOLID186) are used, which significantly increases the calculation time but also the resolution of the result.

Linear 3-node shell elements (SHELL181) are used for governing the element size in the shared partition between the different mesh regions, shown in Figure 4.3. It is necessary to create them before the volume is meshed, using the smallest desired mesh size of the adjacent volumes. With this procedure it is unimportant in which order the individual volumes are meshed. After the final mesh is generated these

SHELL181 elements are deleted. The mesh generation itself is done by an automatic mesh algorithm.

The finest mesh is in the "contact mesh" region depicted in Figure 4.3. The default element edge length in this region is depended on the analysis type. It does not vary within the region itself but for different simulations values between 10 and 100 nm are utilized. The "fine mesh region" is added to achieve a smoother transition to the coarse mesh of the rest of model and to allow a meaningful analysis of the stress in this region. In this region the default element edges are between 100 and 800 nm. The rest of the wafer is meshed coarsely with 1 µm edge length.

On top of the contact region facing in the z-direction are the contact elements CONTA173. Together with their counterpart, the TARGE170 elements, they define the contact behavior. The whole indenter surface is meshed solely with the TARGE170 elements.

4.1.3   Contact Behavior

For the definition of a pair-based contact in ANSYS, as is shown in Figure 4.4, the two element sets of CONTA173 and TARGE170 have to share the same real constants in ANSYS. The contact algorithm is an augmented Lagrangian one and the contact
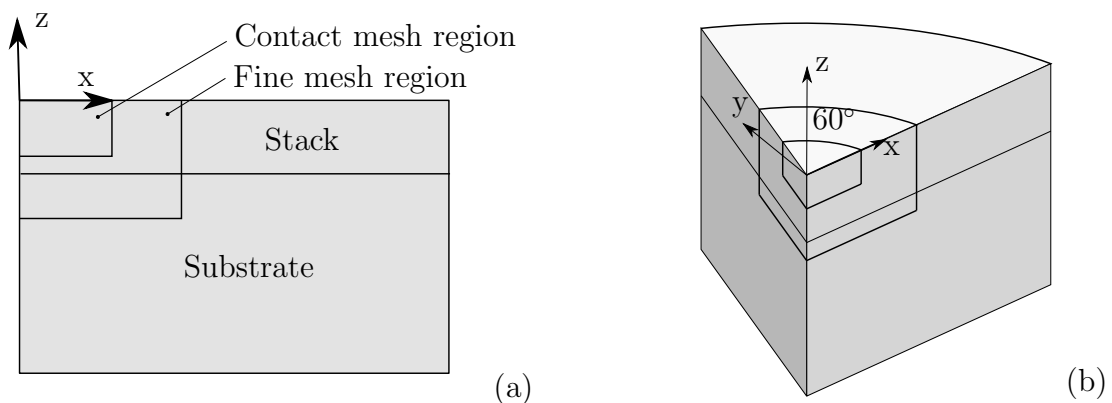
Figure 4.3: The different mesh regions in the xz-plane (a) and in an isometric view (b).

detection points are the nodal points. The force F_c at the contact detection point(s) is calculated by

$$F_c = k_c d_p + \lambda \tag{4.4}$$

whereas k_c is the contact stiffness, d_p is the penetration depth, and λ is an internally calculated term, which enhances the classic penalty-based force calculation. With this term, the solution is more stable and produces less penetration but it also takes more iterations to converge.

The two parameters that are modified to obtain a more accurate solution are the normal penalty stiffness factor (FKN) and the penetration tolerance (FTOLN) as it is explained in the contact technology guide of the mechanical APDL reference [1]. An increased penalty stiffness factor FKN = 5000 is used in the simulations. Such an increased value will lead to less penetration but also needs more iterations to solve and a too high value might not lead to convergence at all. FTOLN is used in connection with the augmented Lagrangian method and defines the absolute allowable penetration, which is for most of the conducted calculations very small, being just 0.1% of the contact element size. If a larger penetration is reached, the convergence criterion for the global solution is never satisfied, even if the residual forces and displacement increments have met convergence criteria [1].
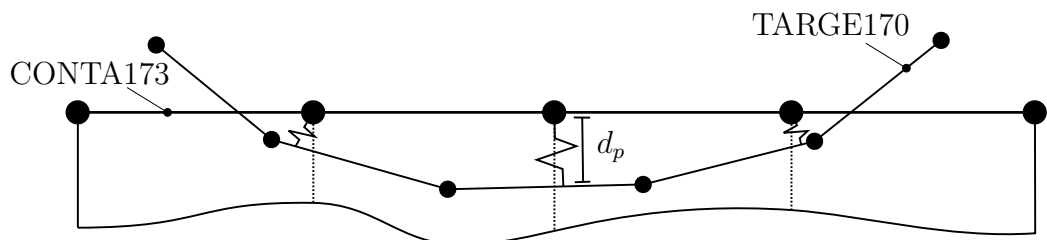
Figure 4.4: Sketch of the used contact model. The TARGE170 model the indenter and the CONTA173 elements the surface of the wafer.

The contact behavior is assumed to be frictionless for the course of this thesis. This
is a common assumption for FEM simulations of Nanoindentation problems [12, 19].

4.1.4   Boundary condition

The boundary conditions of the 3D model are defined in regard to the symmetry
of the problem. The displacement in y-direction is constrained for all nodes in the
xz-plane. To define the boundary conditions of the second symmetry plane a local
coordinate system is created, which is rotated 60° around the z-axis. In this new
$x'z$-plane the boundary condition is then again defined to constrain displacement in
y'-direction. For the bottom plane and the outer border of the model all degrees
of freedom are constrained. A schematic of these boundary conditions is shown in
Figure 4.5.

The boundary conditions of the indenter are used to define the four steps of the in-
dentation procedure. Its initial position is directly above the wafer with one node
already being in contact. In the first step, a displacement boundary condition in
z-direction equal the maximum indentation depth is defined for the indenter. Dis-
placement in the other two directions is restricted. In line with the steps defined
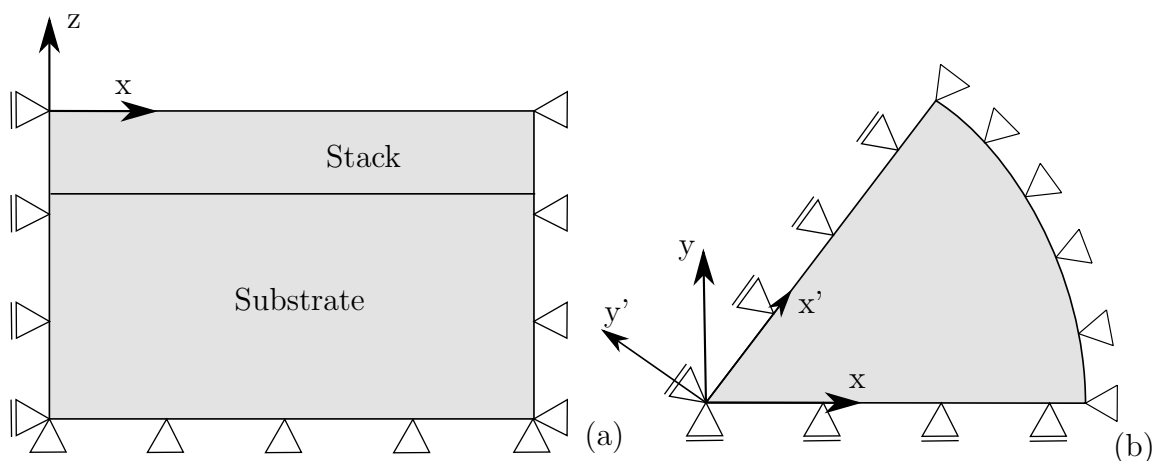
Figure 4.5: The boundary conditions of the wafer and the associated coordinate
systems.

Table 4.1: Direction dependend Young's moduli, Poisson's ratio, and shear moduli of GaN. Young's and shear moduli are given in GPa

Source paper	$E_x = E_y$	E_z	$\nu_{xz} = \nu_{yz}$	ν_{xy}	$G_{xz} = G_{yz}$	G_{xy}
Schwarz et al. [26]	284.4	160	0.21	0.31	81.4	108.5
Polian et al. [23]	324.1	355	0.2	0.32	105	122.5

in Section 1.3 the indenter is subsequently hold for the next load step at the final indentation depth. In the last two steps, displacement boundary conditions are used to withdraw the indenter and hold it at its original position. The two hold steps are not necessary and are just added to model the full experimental procedure. The additional computational effort caused by the hold steps is marginal.

4.2 Material Parameters

The theoretical information necessary to describe the material behavior is already stated in the previous chapters. A summary of this information and how it is used for an appropriate material behavior in ANSYS is presented in this section.

4.2.1 Gallium Nitride Material Parameters

In Section 2.2 the transversely isotropic elastic material parameters given by Schwarz [26] and Polian [23] are explained briefly. To use these material parameters in ANSYS an orthotropic elastic model is defined and set to behave transversely isotropic. The direction-dependent elastic material parameters are given in Table 4.1. The plasticity approach for GaN has already been explained in detail in the previous chapters. The plastic material parameters is shown in Table 4.2.

Table 4.2: Summary of the transversely isotropic plasticity parameters for the GaN layer.

Yield stresses			
$\sigma_{xx}^{Y} = \sigma_{yy}^{Y}$	σ_{zz}^{Y}	$\tau_{xz}^{Y} = \tau_{yz}^{Y}$	τ_{xy}^{Y}
2.79 GPa	7.85 GPa	2.34 GPa	1.41 GPa
Hill Parameter			
$R_{xx} = R_{yy}$	R_{zz}	$R_{xz} = R_{yz}$	R_{xy}
0.355	1	0.516	0.312

Tangent modulus $E_{\mathrm{T}} = 0, 50, 100$ GPa (dependent on analysis)

Table 4.3: Approximated transversely isotropic material parameters given for $\langle 111 \rangle$ Silicon [10, 16] and the tensile yield stress obtained by [22].

$E_x = E_y$	E_z	$\nu_{xz} = \nu_{yz}$	ν_{xy}	$G_{xz} = G_{yz}$	G_{xy}	σ^{Y}
169 GPa	188 GPa	0.182	0.262	66.9 GPa	57.8 GPa	6.9 GPa

4.2.2 Silicon Material Parameters

The face-centered cubic structure of Silicon leads to cubic material behavior. The silicon substrate in the modeled wafer has a $\langle 111 \rangle$ orientation in the z-direction of the geometric model. The interesting aspect of this material orientation is that it is seemingly transversely isotropic, since the Young's moduli, the Poisson's ratio, and the shear moduli are the same for each direction perpendicular to the $\langle 111 \rangle$ axis as is explained by Kim et al. [16]. Calculating the full elasticity matrix shows that coupling terms appear, which are not considered in a transversely isotropic material model. But since the material behavior of the silicon substrate has only a minor role for this thesis the influence of these coupling terms is neglected and a transversely isotropic material model is used as presented in Table 4.3.

One topic which is briefly addressed in this thesis is the plasticity in the silicon substrate. Since silicon is a very brittle material information on its yield onset is sparse. Most commonly the tensile yield strength of 6.9 GPa obtained by Peterson [22] is referenced and it is therefore used in this thesis as an indication if plasticity in the Silicon substrate occurs by assumption of a J2 yield criterion.

4.3 Residual Stress State

In the course of his diploma thesis, Reichel has shown that residual stresses have a large impact on the development of cracks. In the present thesis the influence of these residual stresses on the plasticity in the material and the overall structural response visible in the load-penetration curve is studied. Two different residual stress distributions are examined. The simplified uniform biaxial tensile stress state used by Reichel of 400 MPa in the xy-plane over the whole 1.8 µm stack as it is shown in Figure 4.6 (a) and the more complicated biaxial stress state from [24] shown in Figure 4.6 (b).

As explained in Section 1.4 the results of [24] have been obtained by an ion beam layer removal method in steps of 100nm. For the sake of simplicity not all of the small steps are modeled in the simulation. The used residual stress distribution featuring a reduced number of different stresses is shown in Figure 4.6 (b) as the black line. The stress in in the xy-plane alternates between compression and tension over the stack. For usage in ANSYS initial stresses can be applied to each individual layer. The local self equilibrated stress state corresponds to a global stress free state solved in an initial load step.

4.4 Axisymmetric Nanoindentation Model

Although most of the results shown in the following chapter are obtained using a 3D model, the axisymmetric model represents an important step in the creation of the final model and will, therefore, be explained briefly in this section. In addition, it can be used for simulations of nanoindentations with cono-spherical indenters and for preliminary studies of Berkovich indentation tests.

The meridional section of the axisymmetric model, illustrated in Figure 4.7, has the same width and height equal 32 μm as the 3D model. This geometry is then divided into the required number of stack layers and a fine mesh region is added for the contact and the area of high deformations. The height of the different layers and the size of the contact region is chosen accordingly to the modeled experiment explained in Section 1.4. The geometry of the wafer is meshed with axisymmetric elements
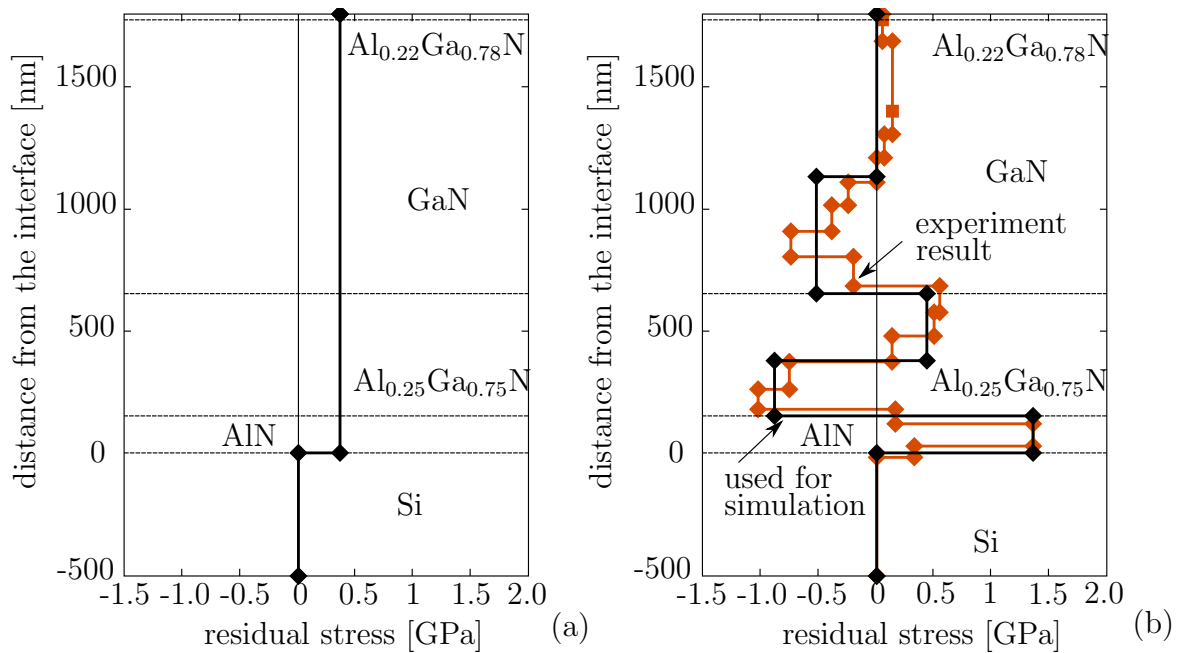

Figure 4.6: Residual stress distribution in the cross-section of the stack. In (a) a homogeneous biaxial tensile stress state of 400 GPa is assumed. Figure (b) shows the results of [24] in red in combination with the biaxial residual stress state used in the simulation in black.

(PLANE183) in a 6-node triangle shape. The usage of this elements define that the y-axis must be the axis of symmetry for the axisymmetric analyses. Therefore, the z-axis in the 3D model corresponds to the y-axis in the axisymmetric model. The mesh size is homogeneous over the largest part of the wafer with a characteristic element length of $0.7\,\mu m$. The only exception is the fine mesh region, which has a standard characteristic element length of $0.08\,\mu m$ and an even finer discretization of $0.02\,\mu m$ at the contact.

The geometry of the nanoindenter is reduced to a line resembling the shape of the indenter. In the case of a conical indenter it is just a straight line which is defined by the included half conical angle. For the cono-spherical tipped indenter its shape is characterized by the radius of the sphere and the angle of the tip. The contact behavior between the wafer an the indenter is realized using a surface-to-surface contact description with TARGE169 elements describing the rigid indenter, which are opposed by CONTA172 elements on top of the wafer. Their properties are equivalent to the one of the 3D model (cf. Chapter 4.1.3).

The boundary conditions are defined as shown in Figure 4.7 to constrain displacement in the x-direction along the y-axis and in the y-direction along the bottom perimeter
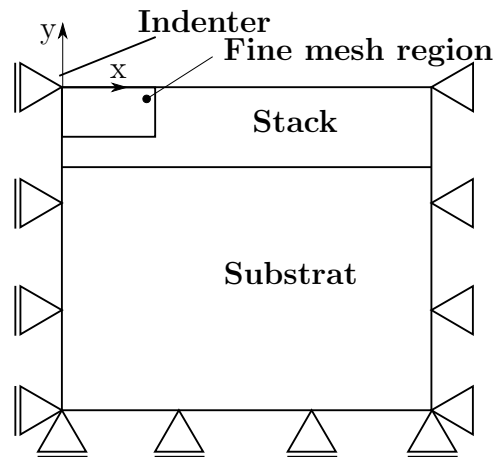
Figure 4.7: Illustration of the axisymmetric nanoindentation model with the different mesh and material regions.

of the model. The indenter is provided with displacement boundary conditions which reflect the indentation procedure explained in Chapter 1.3.

4.5 Verification

To verify that the geometric models and the boundary conditions are applied correctly, they are tested with the material data and the load condition presented in [19]. The model in this paper shares the same load and geometric conditions but has completely different material properties. The load-penetration curves of the axisymmetric and the 3D model of this thesis are hereby very similar to the ones presented in the paper.

Since an important aspect of this thesis is to examine the influence of different parameters on the load-penetration curve numerous simulations are done. The stress distribution in the wafer is not so important for these initial studies, but it is necessary that the computational effort is not too big. Therefore, these simulations are carried out using a linear element formulation and a fairly coarse mesh size.

For the more in-depth stress state evaluation, a computational expensive model featuring quadratic element formulation and a fine mesh size is used. The load-penetration curve obtained with this model shows little to no difference to the one received by the fast calculating model with linear elements.

Chapter 5

Computational Results

In this chapter, the results obtained utilizing the presented FEM models are shown and evaluated. The influence of different material aspects on the shape of the load-penetration curve is examined and the results are compared to the experimental data presented in Section 1.4. A detailed assessment of the simulated Berkovich indenter experiment with an indentation depth of $0.365\,\mu m$ is done, focusing on the contour plots of the resolved shear stresses of various slip systems. The regions where the critical shear stress value is exceeded are located and compared to the region where Hill's yield criterion is fulfilled.

Furthermore, the cono-spherical indenter experiment with the highest indentation depth (cf. Section 1.4) is simulated and the results and the possible applications of the axisymmetric model are evaluated. At the end of this chapter, the question is addressed whether the simulation is capable of predicting the results of further experiments found in the literature.

During the post-processing procedure, the load-penetration data is extracted from ANSYS and visualized via Matlab, whereas the contour plots are created directly in ANSYS APDL.

5.1 Structural Response of the 3D Nanoindentation Model

As explained in Section 1.4, the focus of the simulations is on the experiment, which leads to the load-penetration curves shown in Figure 1.3 (b). This experiment has been carried out with a Berkovich indenter and a maximum indentation depth of $0.365\,\mu m$. To illustrate the global structural response of the 3D model, the reaction force in the z-direction is plotted against the corresponding penetration. It has to be considered that only one-sixth of the structure is modeled, which means that the reaction force has to be multiplied by six.

The load-penetration curve presented in Figure 5.1 is obtained using the elastic parameters by Schwarz [26] (cf. Table 4.1), the presented constants for Hill's plasticity theory (cf. Table 4.2), and a constant tangent modulus of 50 GPa. No residual stresses are used for this simulation. In Figure 5.1 all of the experimental indentations are included, hence 12 partly overlapping curves are printed. The energy dissipation, corresponding to the area under the curve, is a bit smaller for the simulated result but the overall shape of the curve shows an extremely good correlation to the experimental results. Only the small plateau, which is visible at the maximum indentation depth of the experimental results, cannot be simulated by means of this work.

Overall, it is a very satisfactory result considering that the load-penetration curve just describes the overall structural response. A more in detail stress state analysis of this solution will follow later on in this chapter.

5.1.1 Evaluation of Different Elastic Parameters for GaN

Preceding evaluations had to be made to obtain the result, which is shown in the previous section. In the present section, the simulations and considerations are

showcased, which lead subsequently to the conclusion that the elastic parameters by Schwarz [26] are appropriate for this thesis.

Reichel has assumed isotropic elasticity ($E = 290$ GPa and $\nu = 0.26$) for his simulations. As explained in Section 2.2, various transversely isotropic sets of elasticity parameters can be found in the literature, which vary quite significantly. For example, the Young's modulus for the crystallographic {0001} direction, which is equal to the z-direction in the FEM model, ranges between 100 GPa in [30], 160 GPa in [26], and 355 GPa in [23]. From the literature results, Polian's elastic parameters are the most widely used, being cited four times as often as those presented by Schwarz. A strong indication that the chosen elastic behavior is appropriate for the given simulation, is a well-fitting release curve, since, in contrast to the load curve and maximum force, it is determined almost exclusively by the elastic properties.

Figure 5.2 shows one experimental and various simulated load-penetration curves of a Berkovich indentation with a maximum depth of 0.365 µm. The proposed parameters
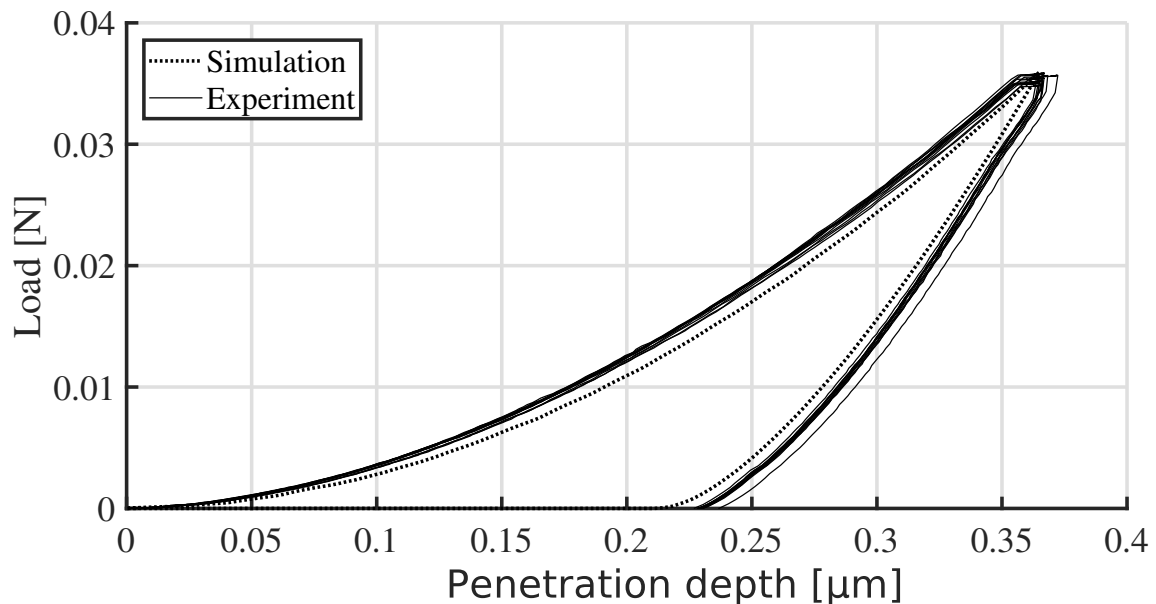
Figure 5.1: Experimental (courtesy of KAI GmbH, Villach, cf. Section 1.4) and simulated load-penetration curves of a Berkovich indentation test with an maximum indentation depth of 0.365 µm. For further details on the simulation please refer to the text (Section 5.1).

for Hill's plasticity theory (cf. Table 4.2) and a constant tangent modulus of 50 GPa are utilized in combination with three different elastic material descriptions. It can be seen that the transversely isotropic elastic parameters by Schwarz depict the experimental load-penetration curve better as Polian's. The isotropic Young's modulus of 290 GPa shows a similar result as Polian's transversely isotropic set of parameters. Both curves exceed the maximum force of the experiment and feature a much steeper release curve.

It needs to be emphasized that all of the literature experiments which have been done to determine the elastic properties have been conducted on bulk material probes, whereas GaN in form of a thin film might feature a different elastic behavior. In addition, the sample stack is in reality not just a single GaN layer instead it has the complex stack design explained in Section 1.4.
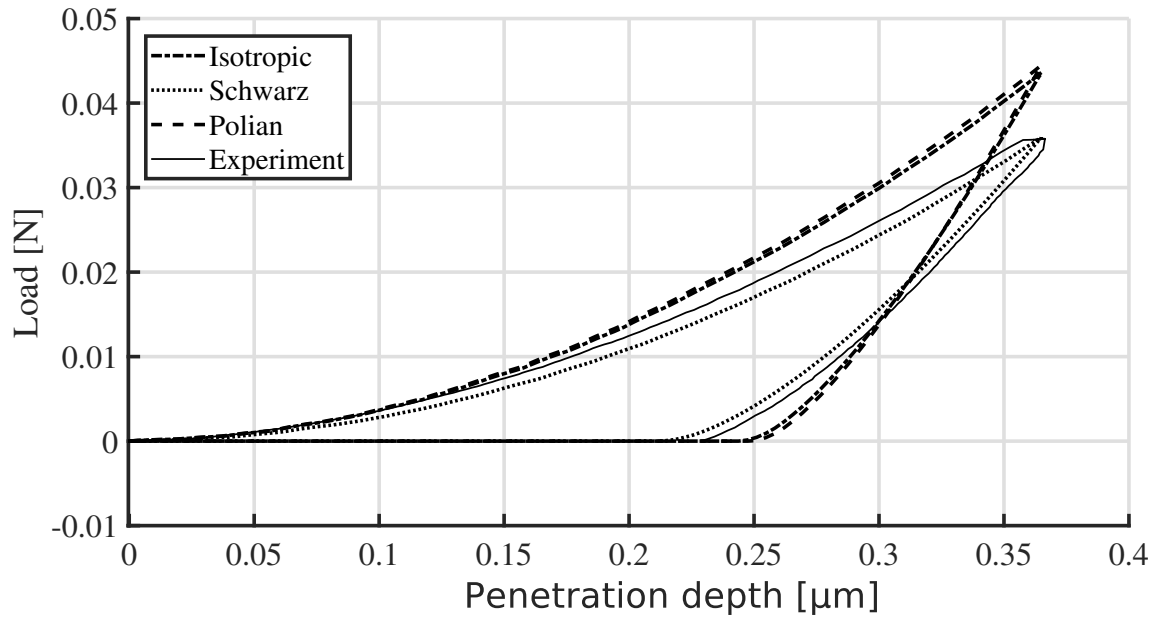
Figure 5.2: Experimental (courtesy of KAI GmbH, Villach, cf. Section 1.4) and simulated load-penetration curves of a Berkovich indentation test. A comparison is made between the transversely isotropic elastic parameter sets, proposed by Polian [23] and Schwarz [26], and an isotropic elastic material behavior ($E = 290$ GPa, $\nu = 0.26$). For further details on the simulation please refer to the text (Section 5.1.1).

In summary, it can be noted that Schwarz's transversely isotropic set of elasticity parameters is well suited for the homogenized stack design and that the elastic properties have to be chosen very carefully for similar simulations.

5.1.2 Influence of the Hardening Behavior

The only information available on the hardening behavior of GaN is found in the compression tests in [30]. However, the statements in this paper are very vague. Therefore, the influence of the hardening behavior is studied. Figure 5.2 shows one experimental and various simulated load-penetration curves. The proposed input for Hill's plasticity theory (cf. Table 4.2) and the transversely elastic parameters by Schwarz [26] (cf. Table 4.1) are combined with different tangent moduli of 0 GPa, 50 GPa, and 100 GPa, to illustrate the influence of the hardening behavior. Figure 5.3 reveals that the tangent modulus of 50 GPa provides the best prediction and that
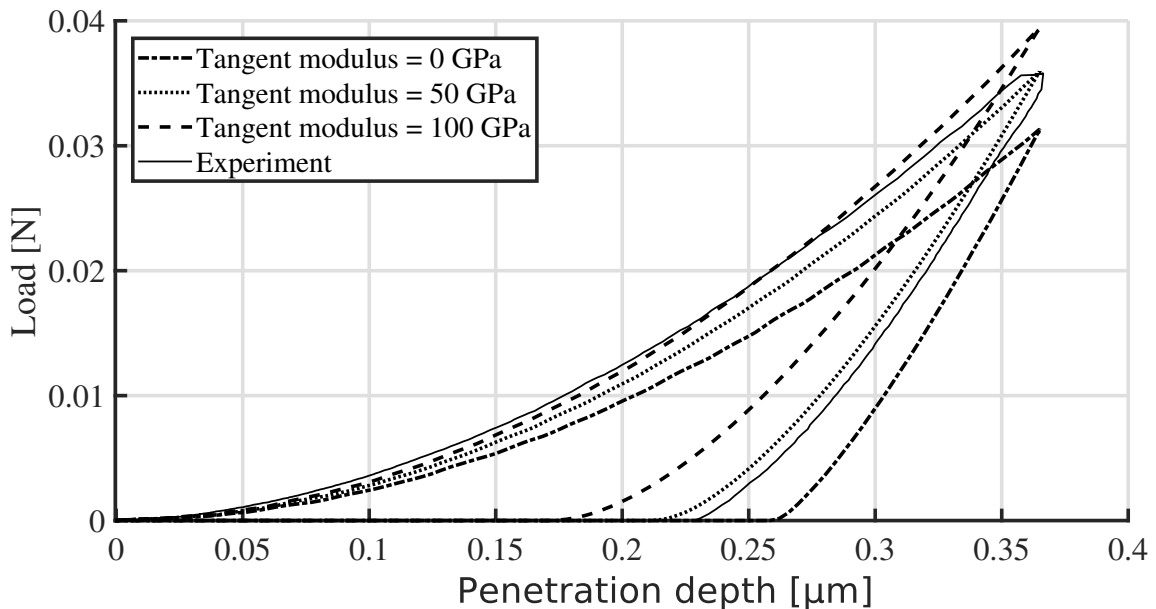

Figure 5.3: Experimental (courtesy of KAI GmbH, Villach, cf. Section 1.4) and simulated load-penetration curves of a Berkovich indentation test. A comparison is made between three different tangent moduli (0 GPa, 50 GPa, and 100 GPa). For further details on the simulation please refer to the text (Section 5.1.2).

the loading step is much more influenced by the plastic properties than the unloading step. As expected, the maximum indentation force of the simulation featuring the tangent modulus of 100 GPa is too high and the one of the ideal plastic simulation is too low.

5.1.3 Plasticity in Silicon

Another aspect which is briefly studied in this thesis is plasticity in the silicon substrate. Whereas the elastic properties of silicon are well-researched (cf. Section 4.2), the information about the plastic behavior is sparse. For this thesis, the tensile yield stress of 6.9 GPa [22] is used as an approximated yield stress for J2 plasticity.

This yield criterion is met in a small area for the simulation presented in Section 5.1. However, simulations combining this approximated J2 yield stress, with an isotropic ideal plastic hardening behavior, show that the effect on the overall structural response of the load-penetration curve and on the stress distribution in the stack is insignificant.

Plasticity in the silicon can, therefore, be disregarded in the simulation for the following detailed stress analyses. Nonetheless, these findings must be taken into account when investigating higher penetration depths. In such a case the plasticity of the substrate might play a significant role in the overall results.

5.2   Stress State Evaluation

To get a better understanding how the plastic deformations are initiated, the previously used load-penetration curves are not sufficient and a more in-depth assessment of the stress state with regard to the different slip planes of GaN is carried out. For this purpose, a post-processing APDL script in ANSYS is used, which automatically creates contour plots of the resolved shear stress in the individual slip systems.

These contour plots allow a fast depiction of the regions in which the critical shear stress values are reached and the dislocation motion has been theoretically initiated. This is realized by using local coordinate systems defined for each slip system. For all of this local coordinate systems, the z'-axis is orientated to be perpendicular to the slip plane in question and the x'-axis is aligned with the considered slip direction. Thereby the local shear stresses $\tau_{x'z'}$ represents the respective resolved shear stress of the corresponding slip systems.

As mentioned previously, there are eleven slip systems which can all occur in multiple orientations, therefore only individual slip directions of selected slip systems are presented in the following sections. A complete presentation of a slip system would have to include all possible orientations (around the z-axis) and a far more complicated post-processing script would be needed to illustrate all of the resulting slip directions in one contour plot.

The considered simulation is the one described in Section 5.1 with Schwarz's [26] elastic parameters (cf. Table 4.1), the proposed parameters for Hill's plasticity theory (cf. Table 4.2), a tangent modulus of 50 GPa, and a maximum indentation depth of 0.365 µm. For this simulation no residual stress state and no Silicon plasticity is used. The critical resolved shear stresses of the slip systems can be found in Appendix A Table A.2.

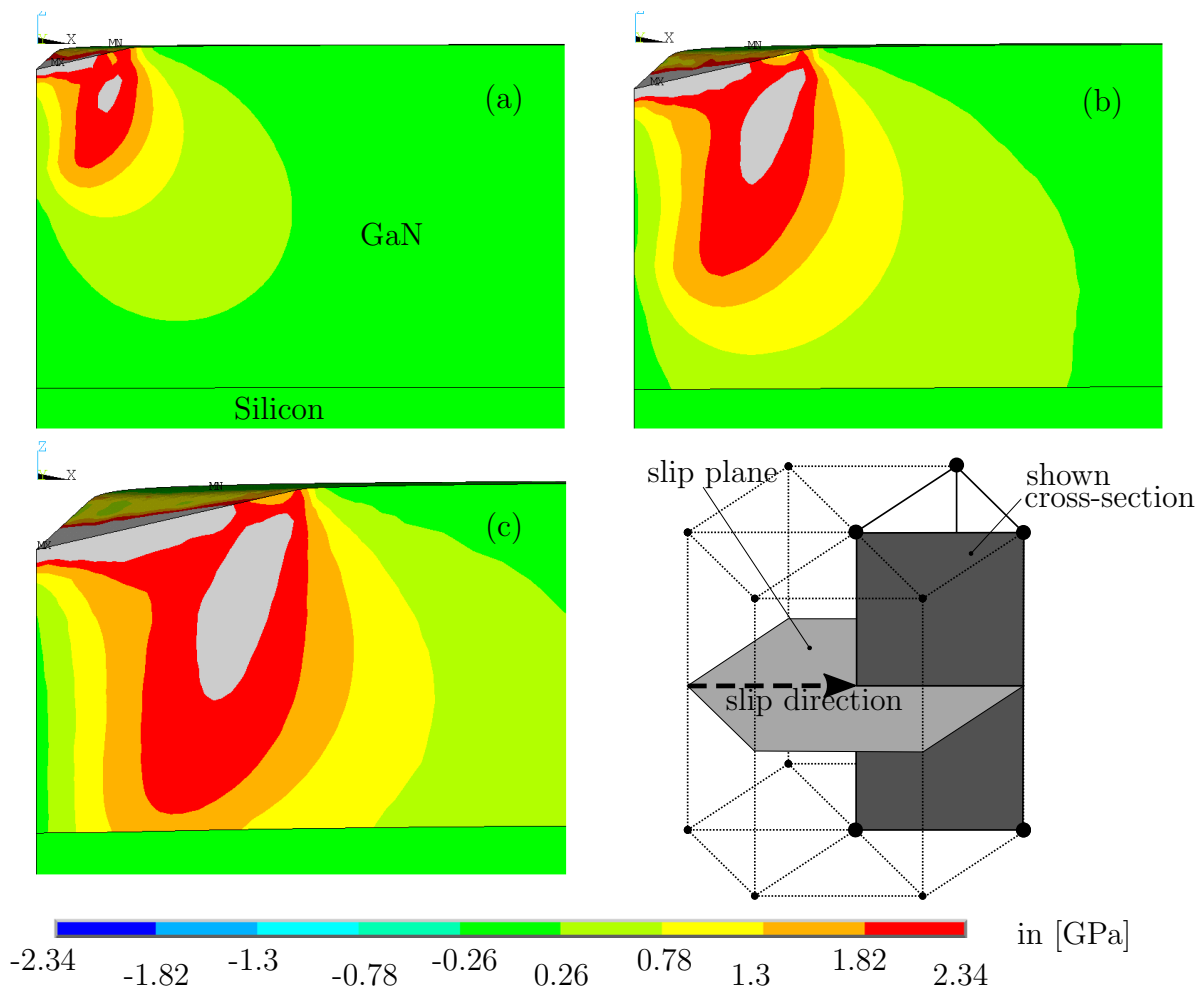## 5.2.1   Resolved Shear Stress in the Basal Plane

Holt and Yacobi [9] state that the predominant slip system to get activated in a Wurtzite crystal structure is the basal plane slip system, since it has the shortest translation vectors. However, there is only one possible orientation for the basal plane in a single crystal, which means that by far not every deformation can be accommodated. Most importantly, normal stress perpendicular to the basal plane cannot cause dislocation motion in the basal plane. Although the translational penetration direction of the indenter is perpendicular to the basal plane, the pyramidal shape of the indenter causes a complex stress state which leads to significant shear stresses in of the basal plane.

Figure 5.4 shows the region in which the critical shear stress in the basal plane ($\tau_{\mathrm{PN}}^{\mathrm{c}} = 2.34\,\mathrm{GPa}$) is exceeded for three different loading states. The region in which the resolved shear stress reaches a higher value than the critical one is marked by the gray area. No local coordinate system is used for this slip direction of the basal plane. The resolved shear stress for the $\langle\bar{1}2\bar{1}0\rangle$ direction is the global τ_{xz} shear stress.

Contour plot (a) shows the resolved shear stress at an indentation depth $u = 0.132\,\mu\mathrm{m}$ (indenter force $F = 0.004\,\mathrm{N}$) and contour plot (b) at an indentation depth $u = 0.201\,\mu\mathrm{m}$ ($F = 0.011\,\mathrm{N}$). The Figure (c) is taken at the final indentation depth ($F = 0.035\,\mathrm{N}$, $u = 0.365\,\mu\mathrm{m}$). The small sketch of the single crystal shows the orientation of the slip system, the slip direction and the cross-section shown in the contour plots. This plane is chosen because it has the largest cross-sectional area of the indenter and cracks are supposed to originate in it.

One can see that the critical resolved shear stress is reached in two different regions during the indentation process. The first region is directly beneath the indenter where the contact leads to a generally high stress state. The second area reaches downward from the perimeter of the contact zone. With increasing indentation depth, the area grows slightly downwards and moves in x-direction.

A careful look at Figure 5.4 (c) raises the question if the region of exceeded critical resolved shear stress has a toroidal shape around the center of the indentation. To answer this question it is necessary to consider the second symmetry plane of the geometric model. Examining the previously assumed slip direction in the second symmetry plane, no region of critical resolved shear stresses can be seen. However, as is presented in Figure 5.5 (a) the second slip direction, rotated by 60°, reaches the critical value in a relatively large region. Figure 5.5 (a) and (b) both show the

Figure 5.4: Contour plots of the resolved shear stress in the basal plane. The gray color marks the area in which the critical resolved shear stress of 2.34 GPa is exceeded. Pictures (a), (b), and (c) show the Berkovich indentation at a penetration depth of $u = 0.132\,\mu\text{m}$, $u = 0.201\,\mu\text{m}$, and $u = 0.365\,\mu\text{m}$, respectively (cf. Figure 5.1).

same simulation at the same maximum penetration depth of $u = 0.132\,\mu m$. The visible cross-section and slip direction is indicated by the sketches above the contour plots. The stress distribution of the second slip direction, shown in Figure 5.5 (a), corresponds to the $\tau_{x'z'}$ of a local coordinate system rotated by 60° around the z-axis.

The critical resolved shear stress region in Figure (a) is larger and extends further in z-direction as the one shown in Figure (b). It is likely, that both regions overlap inside of the 60° segment.
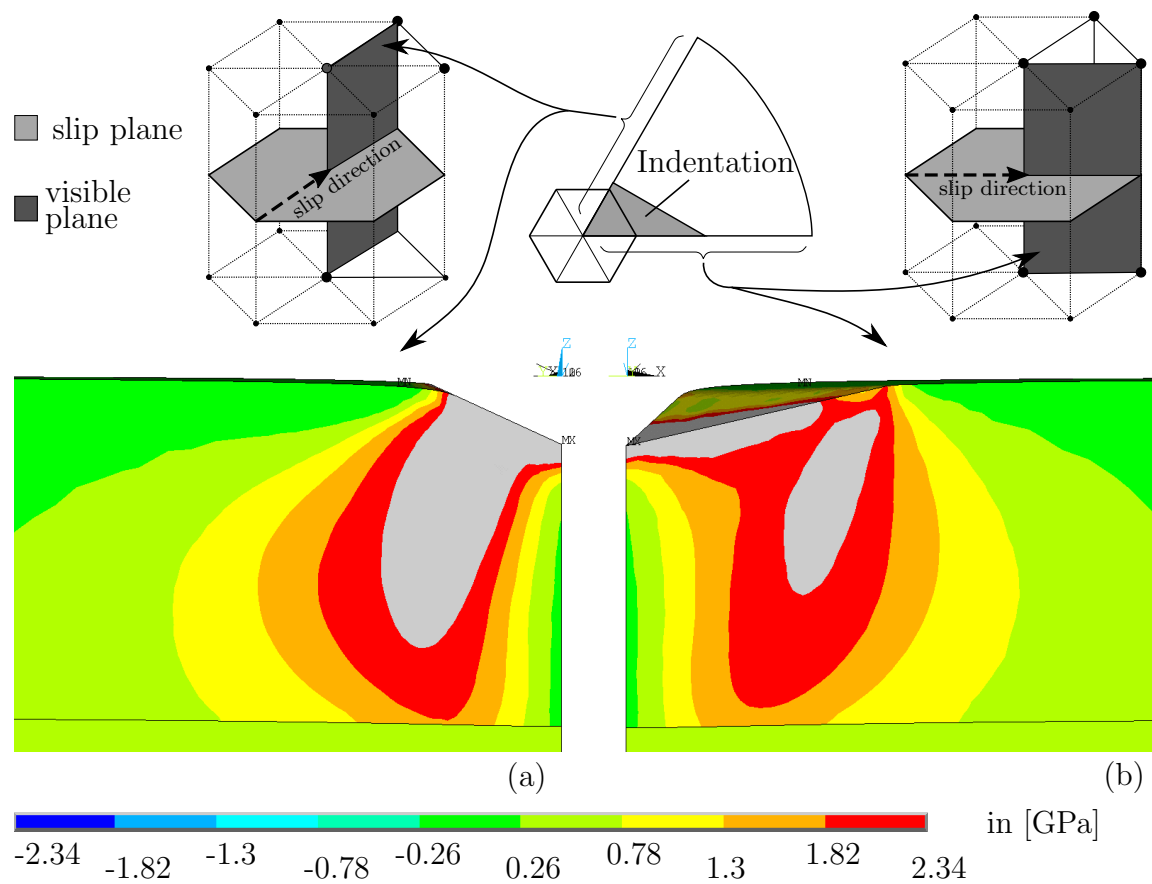
Figure 5.5: Contour plots of the resolved shear stress in the basal plane for the two geometric symmetry planes at the highest indentation depth ($u = 0.365\,\mu m$). The resolved shear stress of two different slip direction orientations is shown in (a) and (b).

5.2.2 Resolved Shear Stress in the Pyramidal $\{1\bar{1}01\}$ Plane

The second slip system to be discussed is the pyramidal $\{1\bar{1}01\}\langle11\bar{2}3\rangle$ system. In contrast to the basal plane, this slip system has a Schmidt factor unequal zero for stress in the z-direction. As explained in Section 2.1 this applies to all three pyramidal slip planes. An interesting aspect of these three slip planes is that their Peierls-Nabarro stresses are really high compared to the basal or the prismatic $\{1\bar{1}00\}$ plane (cf. Table A.2). This is the reason why the experimental values taken from [30] are used in Section 3.1 to define the yield begin in the z-direction and not the Peierls-Nabarro stresses. It is therefore necessary to extract information about the primary active pyramidal slip system from the literature. Caldas et al. [2] and Huang et al. [11] have stated, based on transmission electron microscope and cathodoluminescence microscope pictures, that the $\{1\bar{1}01\}\langle11\bar{2}3\rangle$ slip system is the primary pyramidal slip system, which is activated below the indentation tip.

A local coordinate system has to be used to obtain the contour plots. Therefore the local shear stress $\tau_{x'z'}$ is shown in the following pictures. The local coordinate system is rotated $210°$ around the z-axis and then $62°$ around the $\tilde{y}$-axis to align the z'-axis orthogonal to the slip plane (cf. Appendix A). This slip plane orientation is just one of the six possible orientations in the Wurtzite structure. However, the shape and the size of the critical resolved shear stress region is fairly similar for all six orientations. For the contour plots, a simplification is used regarding the third rotation, which determines the precise orientation of the $\langle11\bar{2}3\rangle$ slip direction. Instead of displaying both possible orientations individually an approximate slip direction which lies between the two orientations is used, which is orthogonal to the second slip direction $\langle\bar{1}2\bar{1}0\rangle$ of this slip plane. With the two mentioned rotations, the resolved shear stress of the approximated slip direction is equal to $\tau_{x'z'}$. The main reason for this simplification is the rotation convention of ANSYS (z-$\tilde{x}$-$\tilde{\tilde{y}}$ Euler convention), which makes it very difficult to orientate the local coordinate system according to the $\langle11\bar{2}3\rangle$ slip direction. The critical resolved shear stress $\tau^{\mathrm{crss}} = 3.25\,\mathrm{GPa}$, corresponding to the

approximate slip direction, is used as an indication for slip initiation in the contour plots.

The resolved shear stress of the simplified slip system is shown in Figure 5.6. The contour plots depict the same simulation and the same load steps as those presented in Figure 5.4. The gray area marks again the region in which the resolved shear stress is higher than the critical one. For this system the region does not expand too
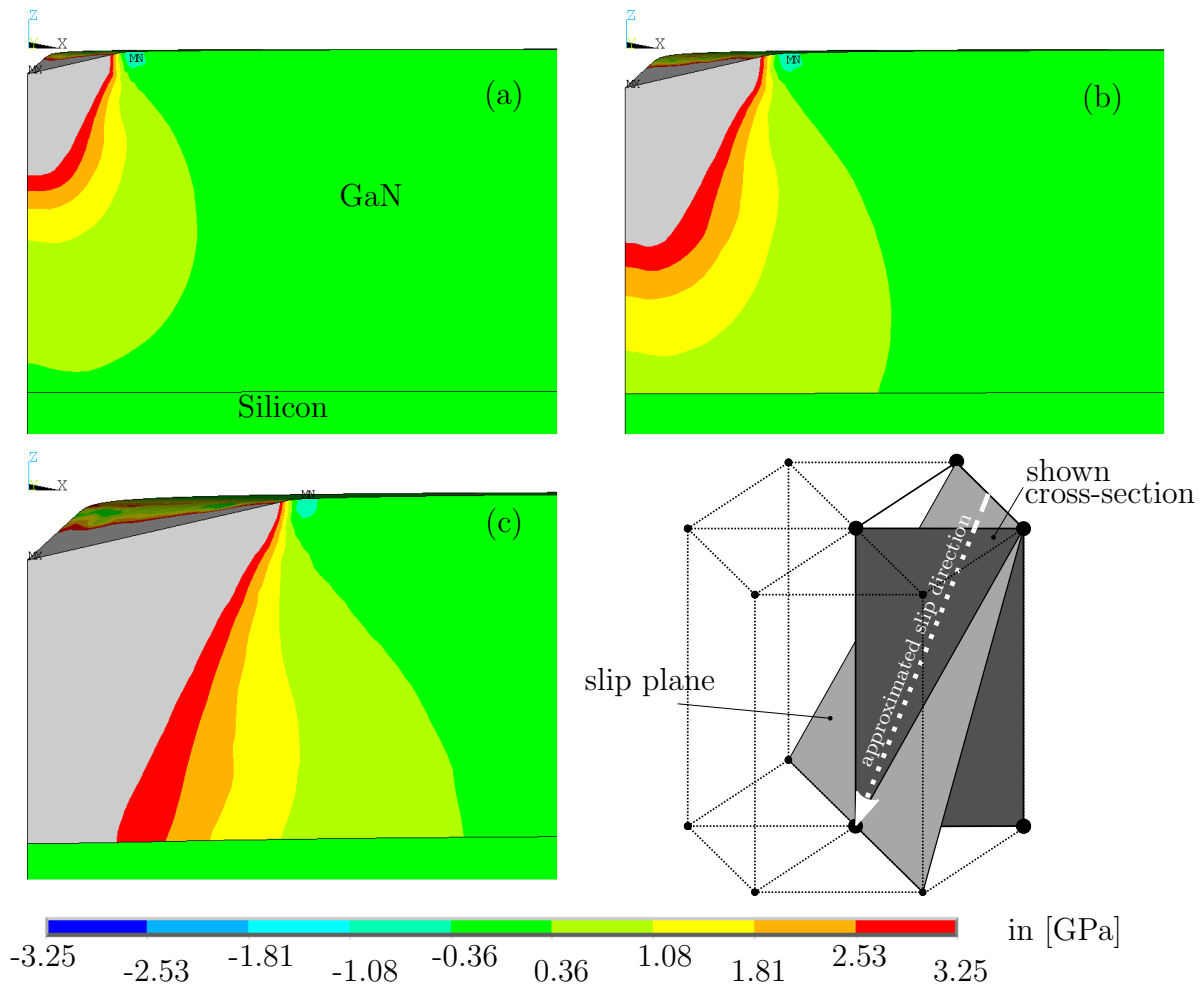
Figure 5.6: Contour plots of the approximated resolved shear stress in the $\{1\bar{1}01\}\langle11\bar{2}3\rangle$ slip system. The gray color marks the area in which the critical resolved shear stress ($\tau^{\mathrm{crss}} = 3.25\,\mathrm{GPa}$) is exceeded. Pictures (a), (b), and (c) show the Berkovich indentation at a penetration depth of $u = 0.132\,\mu\mathrm{m}$, $u = 0.201\,\mu\mathrm{m}$, and $u = 0.365\,\mu\mathrm{m}$, respectively (cf. Figure 5.1).

far in the x-direction, instead, it expands downwards in the direction of the silicon substrate. Compared to critical resolved shear stress region of the basal slip system in Figure 5.4, it can be noted that this area is larger and expands in a different direction.

In Figure 5.6, only one of the two symmetry planes of the FEM model is considered for the stress state analysis of the $\{1\bar{1}01\}\langle11\bar{2}3\rangle$ slip system. Therefore, similar to Figure 5.5, the two planes of symmetry are compared with each other in Figure 5.7. In contrast to the previously shown image, the resolved shear stress of the same slip direction is shown in both planes. One can see that the gray area in which the critical
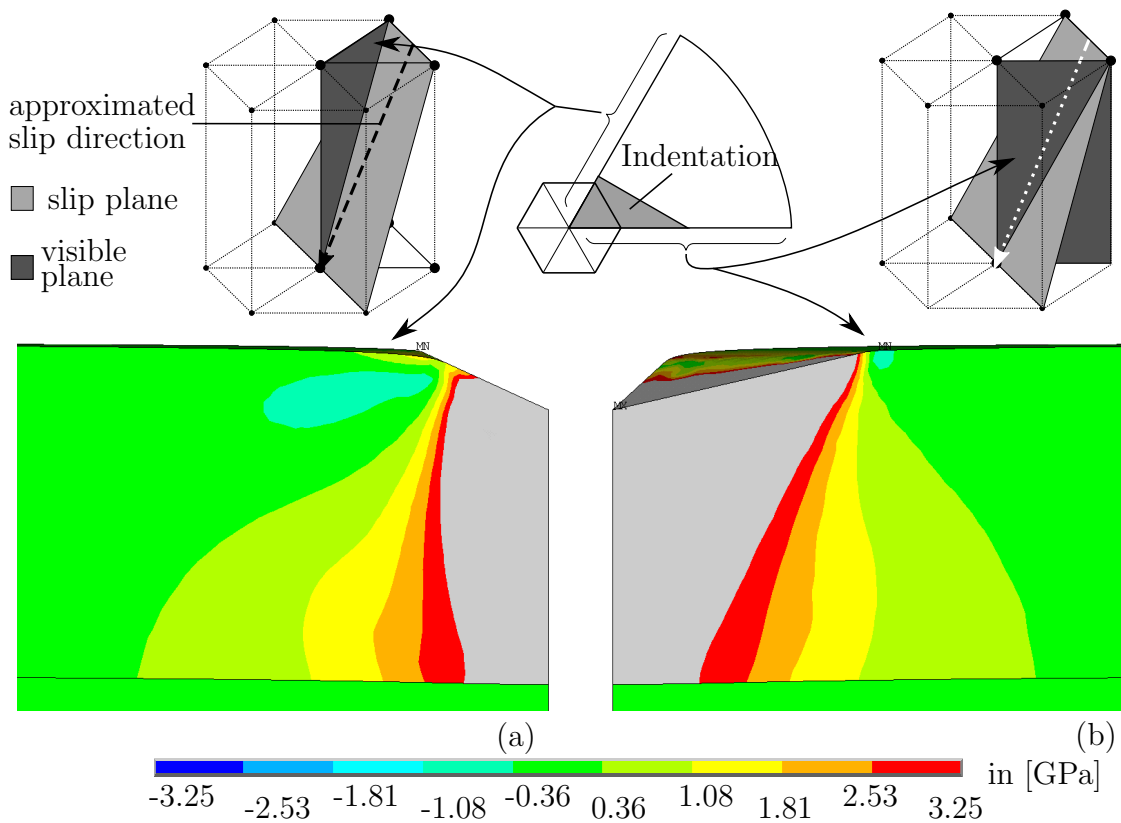
Figure 5.7: Contour plots of the approximated resolved shear stress in the $\{1\bar{1}01\}\langle11\bar{2}3\rangle$ slip system for the two geometric symmetry planes at the highest indentation depth ($u = 0.365\,\mu m$). The resolved shear stress of the same approximated slip direction orientations is shown in (a) and (b).

shear stress of the slip system is exceeded is much smaller in the second symmetry plane depicted in Figure 5.7 (a). Even directly beneath the indenter, the critical value is only exceeded in a smaller area compared to the symmetry plane of the indenter edge shown in Figure 5.7 (b). Examining the critical shear stress regions for the other six slip system orientations reveals that the one presented in Figure 5.7 shows the greatest propagation for both symmetry planes.

5.2.3 Resolved Shear Stress in the Prismatic Plane

The resolved shear stress in the prismatic $\{1\bar{1}00\}\langle\bar{1}2\bar{1}0\rangle$ slip system shows a different aspect of the indentation process as the previously discussed pyramidal $\{1\bar{1}01\}\langle11\bar{2}3\rangle$ system. This prismatic system has similar to the basal plane a Schmid factor of zero for a uniaxial stress state in the z-direction, which means that the quite high stress components σ_{zz} in the global coordinate system have no influence on the resolved shear stresses of this system. This slip system is the one responsible for the yield begin due to normal stress in x and y-direction. However, the normal stress components in the global coordinate system in these directions are relatively small for this load application.

Figure 5.8 illustrates this point quite well. It depicts the shear stress of the $\{1\bar{1}00\}\langle\bar{1}2\bar{1}0\rangle$ slip system in the same simulation then the previously discussed contour plots of the basal and the pyramidal plane. Although the critical shear stress value of this slip plane is just 1.21 GPa and therefore the lowest Peierls-Nabarro shear stress of all systems, the only region in which this value is reached is directly beneath the indenter. It is interesting that the magnitude of the resolved shear stress seems to be similar for both cross-sections. Directly beneath the indentation, there is an even higher resolved shear stress in the cross-section, which is not beneath the indenter edge as can be seen in Figure 5.8 (a). In case of this slip system, no big difference can be seen for the other six orientations of this slip plane. The critical resolved shear stress is not reached for any of the orientations, except directly beneath the indenter.

5.2.4   Comparison to Hill's Yield Criterion

The direct comparison of the critical resolved shear stresses of the activated slip systems and the plastic region of Hill's yield criterion at the highest indentation depth is shown in Figure 5.9. A combination of the previously presented largest critical resolved shear stress regions of the basal and the $\{1\bar{1}01\}$ plane in the xz-plane is depicted in Figure 5.9 (a). The prismatic $\{1\bar{1}00\}\langle\bar{1}2\bar{1}0\rangle$ slip system is not included in Figure 5.9 (a), since the critical resolved shear stress value is only reached directly beneath the indenter. Figure 5.9 (b) illustrates the current reference yield stress σ_0. It is undefined for the silicon substrate, $7.85\,\mathrm{GPa}$ for the dark blue region

(a)   (b)

in [GPa]

-1.21   -0.67   -0.13   0.40   0.94
    -0.94   -0.40   0.13   0.67   1.21
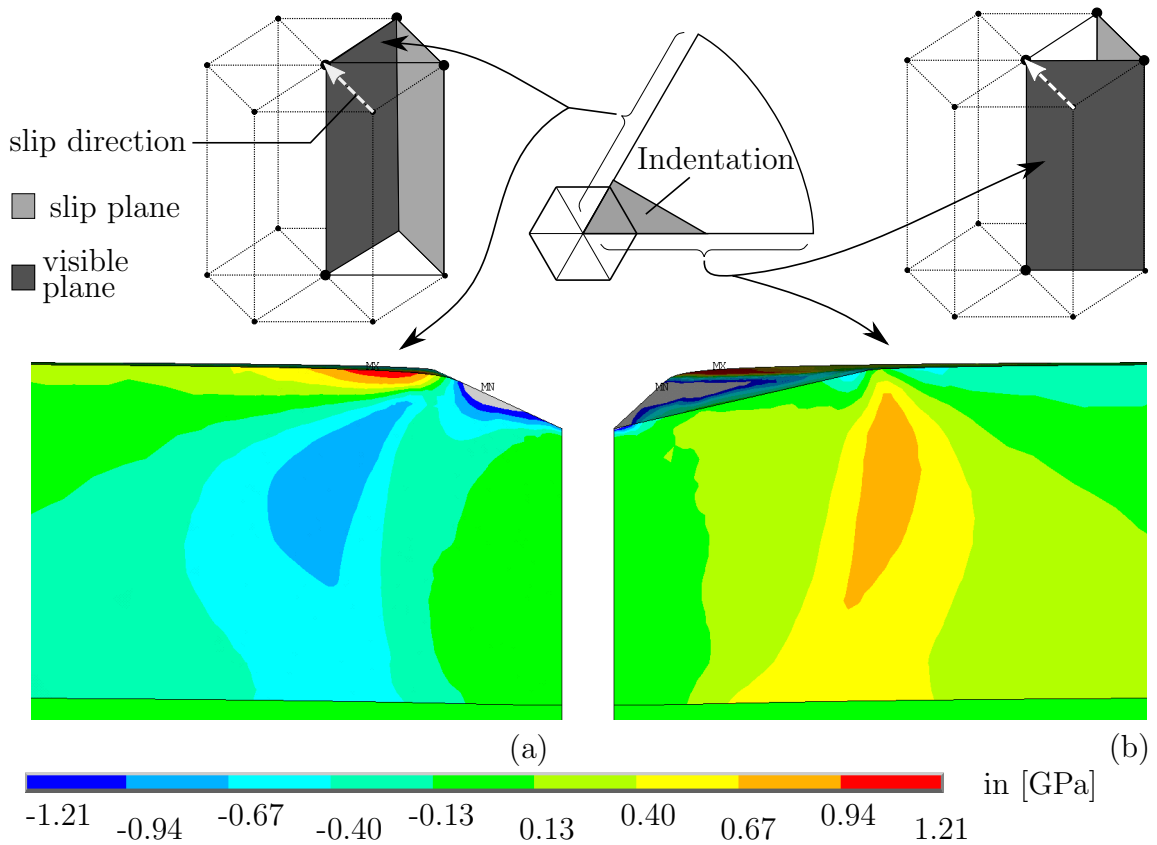
Figure 5.8: Contour plots of the resolved shear stress in the $\{1\bar{1}00\}\langle\bar{1}2\bar{1}0\rangle$ slip system showing the two geometric symmetry planes of the FEM model. Except of a very small region beneath the indenter, the critical shear stress value $\tau_{\mathrm{PN}}^{\mathrm{c}} = 1.21\,\mathrm{GPa}$ is not reached at an indentation depth of $0.365\,\mu\mathrm{m}$.

in which the GaN layer has not been deformed plastically and higher than $7.85\,\mathrm{GPa}$ wherever Hill's yield criterion has been fulfilled and hardening has taken place. This region is larger than the combined residual stress regions seen in Figure 5.9 (a). This is to be expected since Hill's yield criterion is used in a way that it represents all of the slip systems at the same time and not each system separately as does the critical resolved shear stress analyses.

Summarizing the results of this section, it can be said that these evaluations provide important information on the initiation of single crystal plasticity for the presented simulation of the Berkovich nanoindentation model. It indicates that slip occurs in more than one slip system, definitely in the basal plane and in the $\{1\bar{1}01\}\langle1\bar{1}23\rangle$ system. The prismatic $\{1\bar{1}00\}\langle\bar{1}2\bar{1}0\rangle$ slip system has seemingly no large influence on the plastic deformation since critical shear stresses are not reached in this slip system.
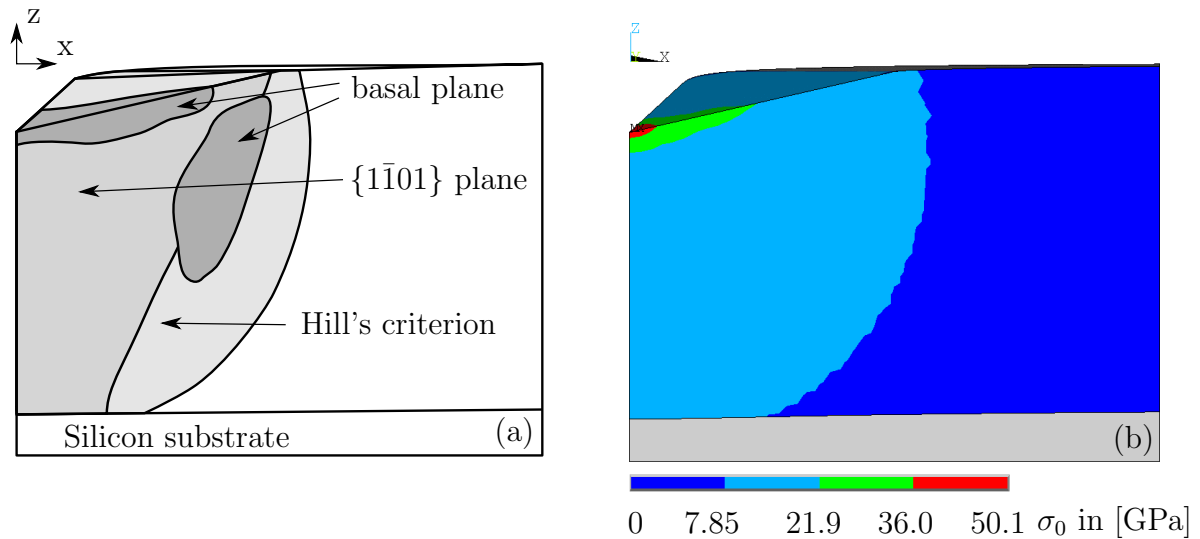

Figure 5.9: A combination of the areas with exceeded critical resolved shear stress of the basal and the $\{1\bar{1}01\}$ plane at the highest indentation depth is shown in (a). In (a), the size of the plastic region of the Hill's yield criterion is also included, which can be comprehended with the current reference yield stress shown in (b).

5.3 Influence of Residual Stresses

The occurrence of production-related residual stresses states in the stack has to be expected, as is explained in Section 1.4 and 4.3. Reichel has shown in his ongoing thesis that these residual stresses have a high impact on the crack initiation and propagation. In this section, the question is addressed whether these residual stresses influence the load-penetration curve and the plastic behavior in general. The following results are therefore obtained with the elasto-plastic model without crack modeling presented in this thesis.

Both residual stress states, presented in Section 4.3, are compared to the simulation without residual stresses. For all three simulations the same elastic parameters by Schwarz [26] (cf. Table 4.1), the same parameters for Hill's plasticity theory (cf. Table 4.2), and the same constant tangent modulus of 50 GPa are used to model the previously discussed Berkovich indentation of 0.365 µm. The load-penetration curves
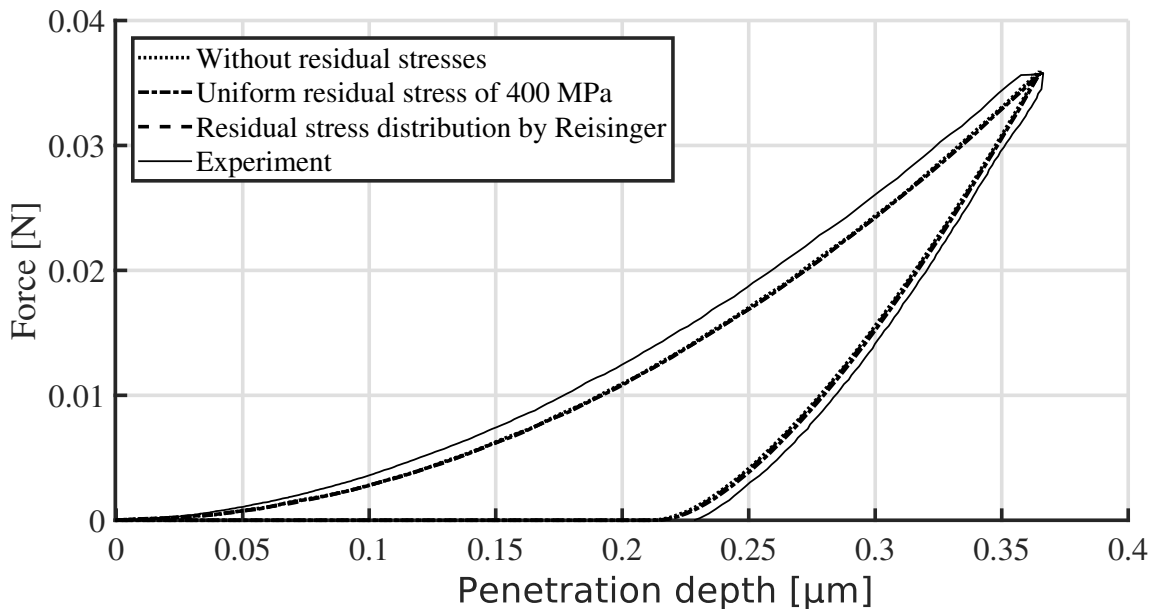

Figure 5.10: Experimental (courtesy of KAI GmbH, Villach, cf. Section 1.4) and simulated load-penetration curves of a Berkovich indentation test. A comparison is made between three different residual stress states. For further details on the simulation please refer to the text (Section 5.3).

are presented in Figure 5.10 and it can be seen that the difference between the three simulations is insignificant.

Neither the uniform stress state with 400 MPa nor the complex stress state (cf. Figure 4.6) have a noteworthy impact on the load-penetration curve. These findings are explained by reconsidering the previously presented results of the $\{1\bar{1}00\}\langle\bar{1}2\bar{1}0\rangle$ slip system. This slip system is important in regard to the biaxial residual stress states because it is responsible for the initiation of plastic deformation due to normal stresses in x and y-direction. The critical resolved shear stress in the $\{1\bar{1}00\}\langle\bar{1}2\bar{1}0\rangle$ slip system ($\tau_{\mathrm{PN}}^{\mathrm{c}} = 1.21\,\mathrm{GPa}$) is not reached with or without either one of the two residual stress cases as it is presented in Figure 5.11. The differences between the different simulations are marginal. The uniform residual stress (Figure 5.11(a)) state shows slightly higher resolved shear stresses compared to the one without residual stresses (Figure 5.11(c)) and for the complex stress state (Figure 5.11(b)) some differences to can be seen at the border to the silicon substrate.

(a)   (b)   (c)

in [GPa]

-1.21   -0.94   -0.67   -0.40   -0.13   0.13   0.40   0.67   0.94   1.21
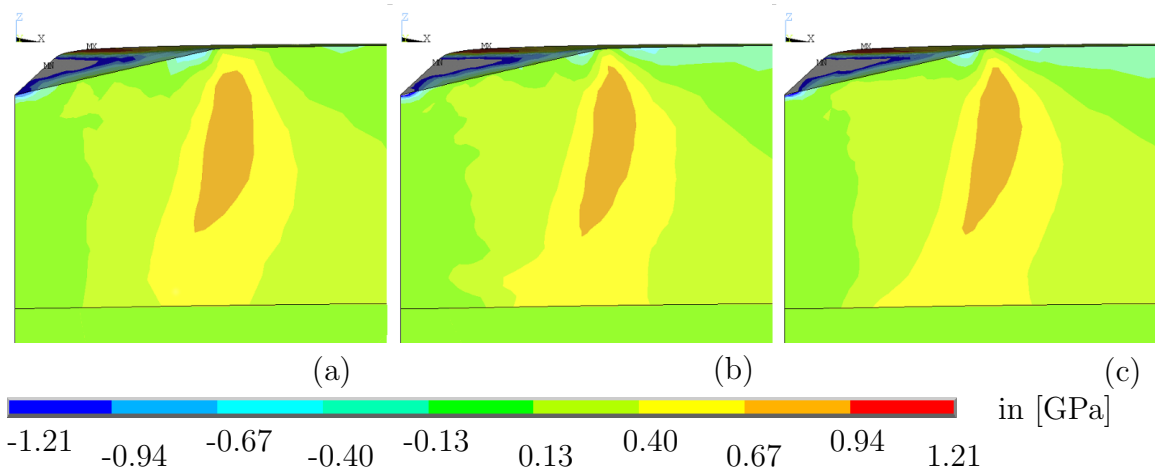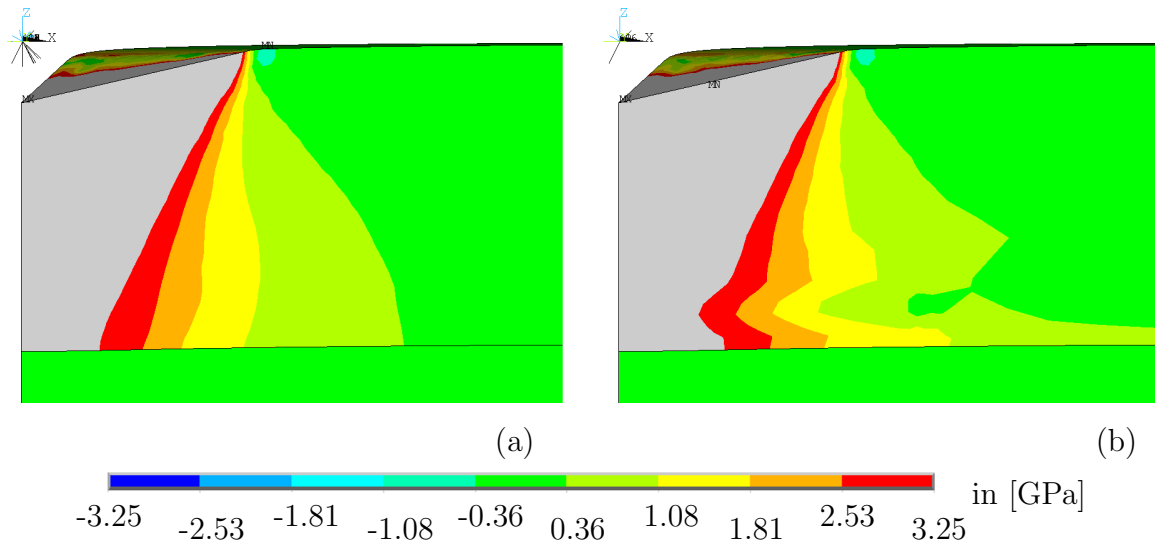
Figure 5.11: Influence of the residual stresses on the resolved shear stresses in the prismatic $\{1\bar{1}00\}\langle\bar{1}2\bar{1}0\rangle$ system. Figure (a) is obtained with the uniform stress state of 400 MPa, Figure (b) shows the result utilizing the complex stress state of Reisinger et al. [24], and Figure (c) depicts the result without a residual stress state.

The influence of the complex residual stresses state on an already activated slip system is depicted in Figure 5.12 using the $\{1\bar{1}01\}\langle11\bar{2}3\rangle$ slip system as an example. Figure 5.12 (a) shows the simulation without residual stresses and Figure 5.12 (b) the simulation with the complex residual stress state. Again, the gray region represents an exceeded critical resolved shear stress. The difference between residual tension and compression stress states is hereby visible. In the area of the compression stress state the resolved shear stress is smaller and vice versa it is bigger at the tension stress state.

5.4 Cono-spherical Indenter

As explained in Section 1.4, experiments using a cono-spherical indentation tip with a radius of 2 µm have been conducted in addition to the Berkovich indentation experiments. In line with the Berkovich simulation, the experiment with the highest indentation depth is simulated.

(a)   (b)

in [GPa]
-3.25   -2.53   -1.81   -1.08   -0.36   0.36   1.08   1.81   2.53   3.25

Figure 5.12: Contour plots of the resolved shear stress in the $\{1\bar{1}01\}\langle11\bar{2}3\rangle$ slip system at the highest indentation depth. The simulation with residual stresses is shown in Figure (a) whereas Figure (b) depicts the simulation with the complex stress state of Reisinger et al. [24].

In Figure 5.13, it can be seen that during the loading process the experimental and the simulated load-penetration curves differ from each other. Nevertheless, the simulation achieves a similar maximum force as measured in the experiment and the release curve fits quite well. For the simulation, the usual parameters for Hill's plasticity theory (Table 4.2), a tangent modulus of 50 GPa, Schwarz's elastic parameters (Table 4.1), and no residual stresses are used.

The pop-in event occurs much later in the indentation procedure of the cono-spherical indentations and significantly stronger, as for Berkovich indentations. The late occurrence of the pop-in event cannot be reproduced with the means and the scope of this thesis.
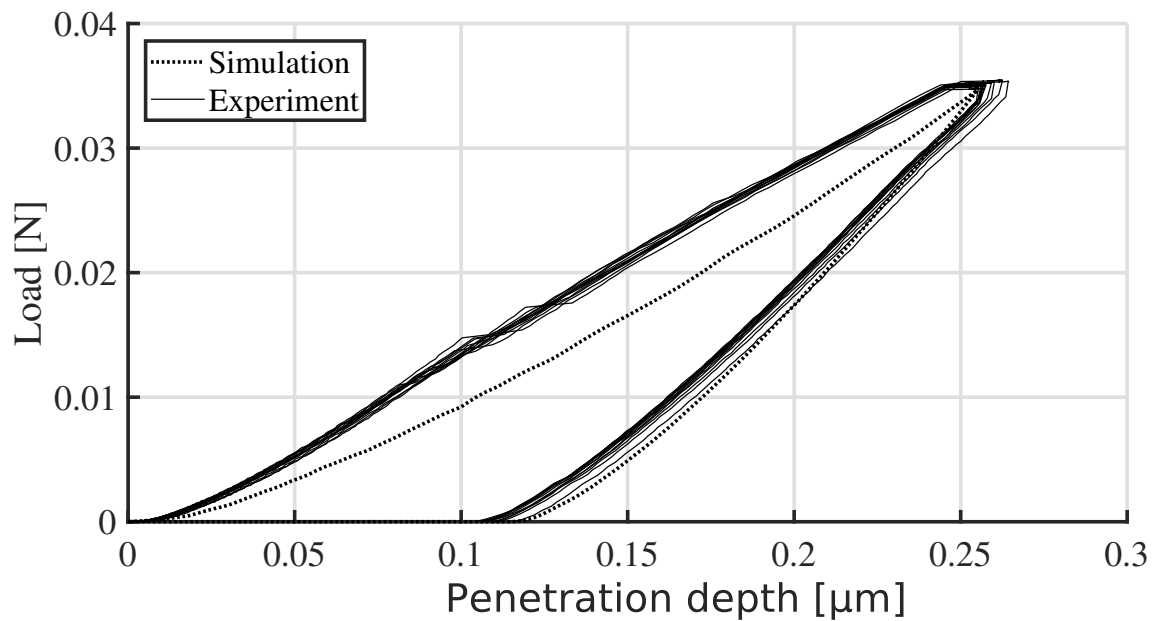
**Figure 5.13:** Experimental (courtesy of KAI GmbH, Villach, cf. Section 1.4) and simulated load-penetration curves of an indentations using a cono-spherical indenter with a radius of 2 μm. The maximum indentation depth is 0.265 μm. For further details on the simulation please refer to the text (Section 5.4).

5.5 Axisymmetric Model

Although all of the previously presented results are obtained utilizing the 3D model, the axisymmetric model presented in Section 4.4 has an important benefit for the simulation procedure, i.e. the shorter calculation time. It is therefore used in this thesis to make preliminary calculations allowing to estimate the result for the 3D model and to perform less precise but faster studies of experiments presented in papers.

The interesting aspect hereby is how different the results of the axisymmetric model and the 3D model are. Figure 5.14 shows the result of a direct comparison of the two models. The indentation utilizing a cono-spherical indenter is shown in Figure 5.14 (a) and the one with a Berkovich indenter in Figure 5.14 (b).

The comparison of the two modeling approaches shows a quite good correlation. For the cono-spherical indenter, the difference between the axisymmetric simulation and 3D simulation is negligible. For the indentation with a Berkovich indenter, a small but notable difference can be seen. The 3D model has a stiffer indentation curve and
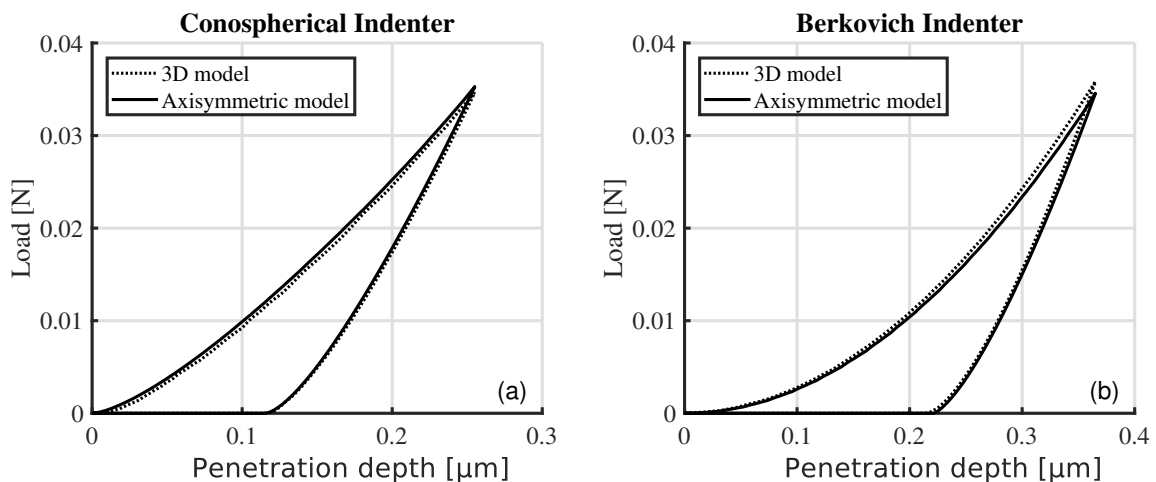
Figure 5.14: Comparison of load-penetration predictions of the 3D model and the axisymmetric model with two different indenter types. Figure (a) shows an indentation with a cono-spherical indenter whereas (b) compares the two models with a Berkovich indenter.

a higher maximum force as the one of the approximated axisymmetric indenter. The differences can hereby be attributed to the approximated indenter geometry of the axisymmetric model as explained in Section 4.1.1. This can also be seen clearly in Figure 5.15 which show the critical resolved shear stress region of the basal plane at the highest indentation depth ($u = 0.365\,\mu m$). Figure 5.15 (a) and (b) shows the previously discussed comparison of resolved shear stress in the two symmetry planes of the 3D model (cf. Figure 5.5). The result of the axisymmetric model is depicted in Figure 5.15 (c). The material properties are the same for both simulations with the usual parameters for Hill's plasticity theory (Table 4.2), a tangent modulus of 50 GPa, Schwarz's elastic parameters (Table 4.1) and no residual stresses. The region of critical resolved shear stresses has for the axisymmetric model approximately the same size as for the symmetry plane of the 3D model depicted in Figure 5.15 (a), whereas the second symmetry plane (Figure 5.15 (b)) has a smaller region of exceeded shear stress.

Overall, it can be said that the usage of the axisymmetric model as a first approximation is viable for a Berkovich indentation as long as the main interest is the structural

(a)   (b)   (c)

-2.34   -1.82   -1.3   -0.78   -0.26   0.26   0.78   1.3   1.82   2.34   in [GPa]
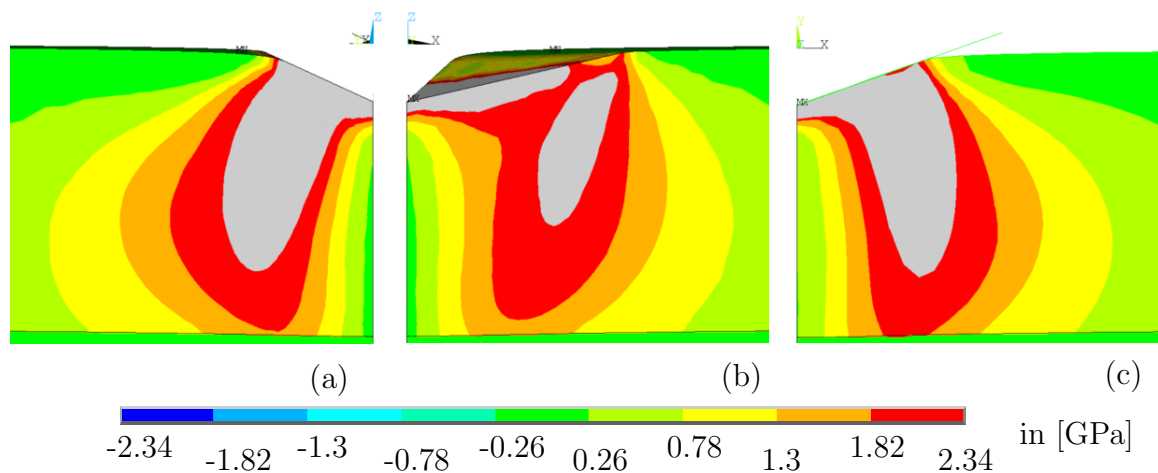
Figure 5.15: Resolved shear stress distribution in the basal plane for two symmetry planes of the 3D Berkovich model (a) and (b) and the approximated axisymmetric model (c) which has a conical indenter with the same contact area. For further details on the simulation please refer to the text (Section 5.5).

response in form of the load-penetration curve. To evaluate the stress distribution of an indentation with a Berkovich indenter, the 3D model should be used. In the case of the cono-spherical indenter, the solution is as good as the 3D model.

5.6 Comparison to Literature Results

So far, the results of the indentation experiments conducted at the KAI GmbH are examined and discussed. To understand how good this simulation approach works for different nanoindentation experiments, the model is used to simulate results found in the literature.

It has to be mentioned beforehand that a comparison between the results of various papers shows that the mechanical properties of GaN depend on the production process. For example, trace impurity elements are commonly and intentionally inserted into GaN wafers during a procedure process called doping, to modify the electrical properties and to influence the crystal growing procedure [30]. It is reported that this process affects the mechanical properties [5, 15].

5.6.1 Comparison to the Results of Huang [11]

The first experiment chosen to be simulated is the one published by Huang et al. [11]. This paper contains cathodoluminescence microscope pictures of the activated slip systems, which are interesting with regard to the critical resolved shear stresses visualized in the contour plots. For this experiment, a cono-spherical indenter with a radius of $5\,\mu m$ has been used.

In [11] no information on the doping procedure is given which can imply that the material is undoped or that the doping configuration is just not published. The tested sample is a GaN single crystal. Figure 5.16 shows the experimental results of [11] and a simulation with the axisymmetric model. Schwarz's [26] elastic parameters are again combined with the proposed parameters for Hill's plasticity theory (cf. Table

4.2), but instead of the hitherto used tangent modulus of 50 GPa, an ideal plastic behavior is assumed in this case. Since a cono-spherical indenter has been used in the experiment the simulation is done with the axisymmetric model.

The simulation of this experiment reveals that the material parameters which work quite well with previously discussed KAI experiments do not fit that well in this case. In Figure 5.16, it becomes apparent that despite the ideal plastic material assumption, the simulation leads to a stiffer material response than the experiment. The release curve of the experiment is less steep than the one of the simulation, which indicates that the already relatively compliant elastic parameters by Schwarz [26] are too stiff.

The cathodoluminescence microscope pictures published in this paper allow to draw conclusions on the slip systems which get activated during the indentation. Figure 5.17 (a) is taken from [11] and shows the slip bands as black lines. Most of these are orientated in three different directions. The ones parallel to the sample surface indicate slip in the basal plane. They appear mostly to the side of the indentation.
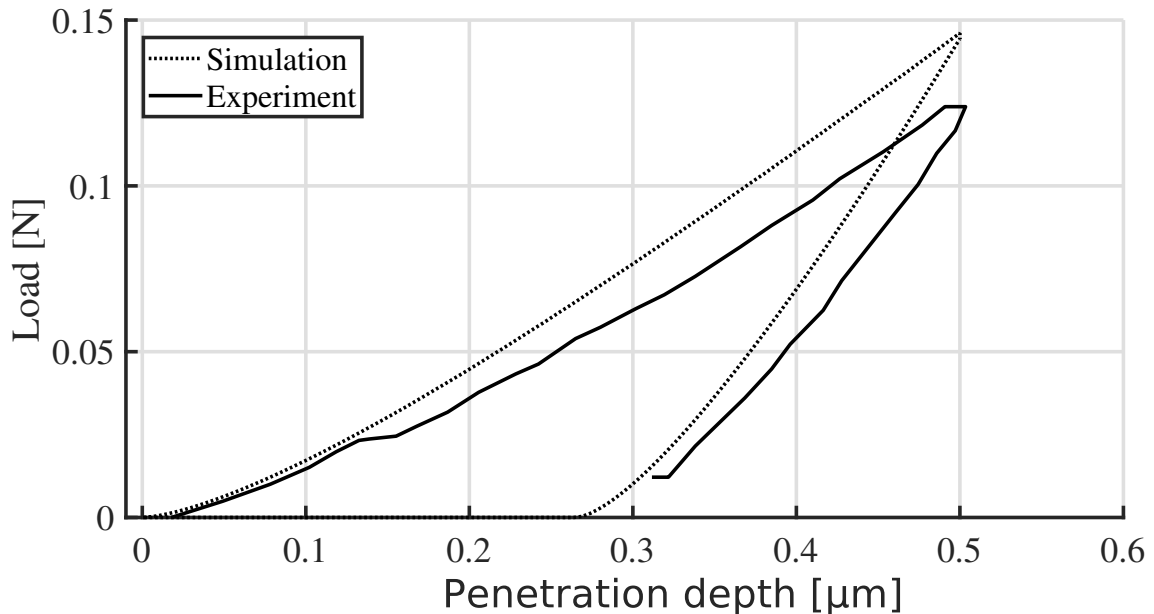
Figure 5.16: Experimental [11] and simulated load-penetration curves using a cono-spherical indenter with a radius of 5 μm. A maximum indentation depth of 0.5 μm is reached. For further details on the simulation please refer to the text (Section 5.6.1).

The inclined slips beneath the indenter show angles of 58° and 95°, respectively. Both of these angles have been attributed to the $\{1\bar{1}01\}\langle11\bar{2}3\rangle$ system by the authors (cf. Figure 5.17 (b)).

Figures 5.17 (c) and (d) show the corresponding contour plots of the simulation. The regions in which the resolved shear stresses reach a higher value than the critical ones are marked by the gray areas. Figure (c) illustrates the approximated $\{1\bar{1}01\}\langle11\bar{2}3\rangle$

-3.25 -1.81 -0.36 0.36 1.81 3.25 in [GPa]   -2.34 -1.30 -0.26 0.26 1.30 2.34 in [GPa]
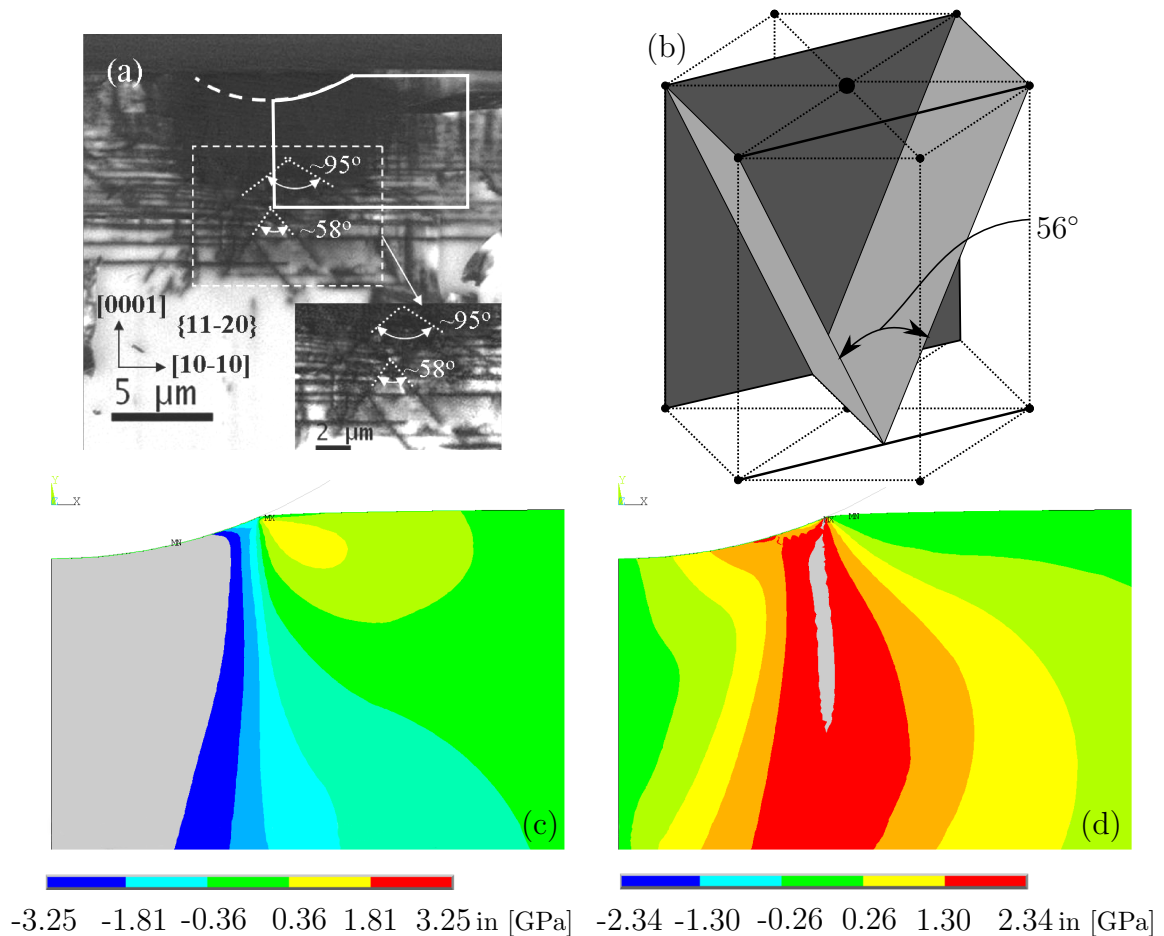
Figure 5.17: Figure (a) shows the cathodoluminescence microscope pictures of [11]. The angles between the pyramidal slip planes visible in this picture can be found in the schematic representation of slip system $\{1\bar{1}01\}\langle11\bar{2}3\rangle$ depicted in Figure (b). The solid white box in (a) corresponds to the in (c) and (d) depicted contour plots. Figure (c) shows the resolved shear stress in the pyramidal $\{1\bar{1}01\}\langle11\bar{2}3\rangle$ system and Figure (d) depicts the resolved shear stress in the basal plane.

system and Figure (d) the basal slip system. The section of the GaN probe shown in Figures (c) and (d) matches approximately the region marked with the thick white solid line in Figure (a). It is difficult to make distinct statements because the picture is relatively dark, but one can see that most of the pyramidal slips occur beneath the center of the indenter, as it is predicted by the contour plots. The slips in the basal plane extend far to the side of the indentation in the microscope picture, whereas the contour plot shows only a very small area of critical resolved shear stress in Figure 5.17 (d). In order to further analyze these differences, it would be necessary to know more about the experimental setup and the used material.

5.6.2 Comparison to Further Papers

As is described in Section 1.2 various other authors have done experiments utilizing Berkovich indenters. Two more Berkovich indentation experiments are simulated to allow for a better assessment of the capabilities of the proposed modeling strategy. For this purpose, the results of Nowak et al. [21] and Tsai et al. [27] are selected. The experiments have a maximum penetration depth of 0.16 μm and 0.12 μm, respectively, and the main difference between the two experiments is that in [21] bulk material has been tested whereas in [27] a 2 μm thin GaN film on sapphire has been used.

The load-penetration curves are shown in Figure 5.18. The material parameters of GaN are the same for both simulations with the proposed parameters for Hill's plasticity theory (cf. Table 4.2), a tangent modulus of 50 GPa, and Schwarz's [26] elastic parameters (cf. Table 4.1). The simulation results are obtained using the axisymmetric model since only the general response is of interest. A discrepancy between the simulation and the experiments can be seen for both cases. This discrepancy is stronger for Figure 5.18 (a) depicting the experimental results of [21] then it is for the results of [27] presented in Figure 5.18 (b).

Both results show a stiffer material response for the experiments as for their simulated counterpart. This is contrary to the findings presented in Section 5.6.1, in which the

experimental result has a less stiff material response. Moreover, the response of the bulk material seen in Figure 5.18 (a) is stiffer as the one of the GaN film structure (b). This difference is not reflected in the simulation, although the sapphire substrate is modeled with the appropriate elastic material parameters, which can be found in [4]. The 2 μm GaN layer is too thick, as that the sapphire substrate influences the load-penetration curve significantly in the simulation.

Similar to the results of the KAI experiments, the simulated release curve shows a slope which matches the experiment, which means that the differences occur mainly due to the chosen plasticity parameters of the simulation. A higher reference yield stress or a stiffer hardening behavior could lead to a better fitting result. This demonstrates that the proposed approach works in principle quite well but it has to be evaluated for each individual stack design independently.
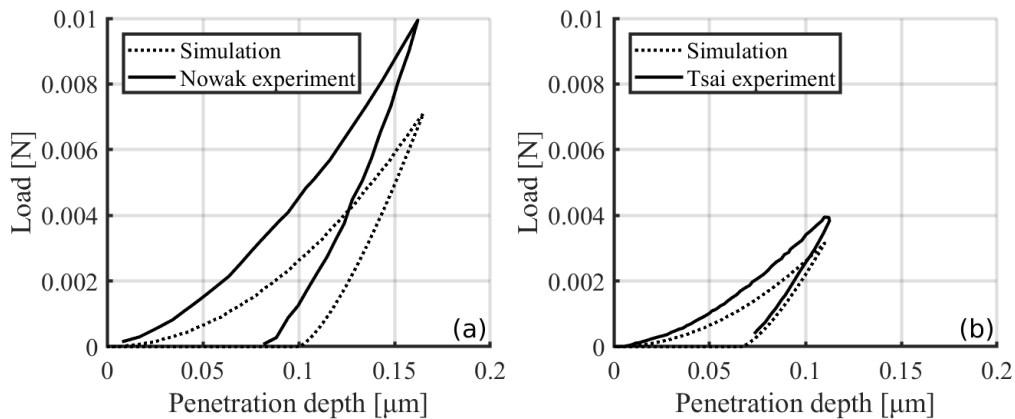
Figure 5.18: Simulation of the experimental result by Nowak [21] (a) and Tsai [27] (b). The simulations are done with the approximated Berkovich indenter in the axisymmetric model.

Chapter 6

Conclusion and Outlook

In this last chapter, a short summary of the achieved results is given and the most important findings are highlighted. Furthermore, the problems which are connected with the modeling of Gallium Nitride are addressed and thoughts on further studies are given.

6.1 Conclusion

The main goal of this thesis is to find a modeling approach capable of simulating the elasto-plastic response of nanoindentation experiments of GaN on Silicon Wafers, as they are conducted at the industrial competence center KAI. To be able to address the direction dependencies of the single crystal GaN structure a modeling approach utilizing Hill's plasticity theory is proposed. This approach is based on the idea that the critical shear stresses of the individual slip planes can be used to determine transversely isotropic Hill parameters. For this purpose, experimental yield stress values [30] and theoretical Peierls-Nabarro critical shear stresses [2] are used. A constant tangent modulus is applied to describe the isotropic hardening behavior. To verify that it responds as expected, the approach is tested via single element simulations. These tests have quite satisfactory results.

The simulation of the KAI Berkovich nanoindentation experiments shows an exceptionally good correlation between experimental and simulated load-penetration curves. During the evaluation process preceding this simulation, two sets of transversely isotropic elastic parameters and an isotropic material model are compared and three different tangent moduli are tested. These evaluations lead to the utilization of the transversely isotropic elastic material parameters, proposed in [26] and a tangent modulus of $50\,\mathrm{GPa}$.

To get a better understanding of the initiation of plastic behavior in the GaN layer, the resolved shear stresses of the individual slip systems are visualized in form of contour plots. These contour plots indicate that the basal plane, as well as at least one of the pyramidal planes, are activated during the indentation process. In the prismatic slip planes, the critical resolved shear stresses are not exceeded.

The effect of production-related residual stress states due to the lattice mismatch of GaN and Silicon is studied. Therefore, the influence of two different residual stress states on the load penetration curve and on the critical resolved shear stresses of selected slip systems is examined. Overall the visible effects of residual stresses are very limited. Virtually no impact could be seen on the load-penetration curves and only very small changes in the resolved shear stresses.

Furthermore, a KAI experiment with a cono-spherical indenter is simulated utilizing the proposed material properties. The strong and rather late appearing pop-in events visible in the experimental load-penetration curves of this experiments cannot be reproduced in the simulation. They represent a strong nonlinear behavior which is outside the scope of this thesis. Nevertheless, the maximum indentation force and the release curve of the simulation fits the experimental ones. Regarding the simulation of experiments found in the literature, it is obvious that the material properties of GaN are depended on the production process and the probe design, i.e. whether it is a bulk material or has a wafer structure. Despite these difficulties, it is possible to see a correspondence between the slip systems which reach critical shear stresses in the simulation and the active ones reported in the literature. The results of further

nanoindentation simulations show a higher discrepancy compared to the associated experimental load-penetration curves.

In summary, the modeling approach for single crystal plasticity has great potential and its use results in a well correlating simulation of the Berkovich indentation experiments of GaN on Si wafers carried out at the KAI. In addition, the analysis of the individual slip system allows conclusions to be drawn on their activation. The results of these stress state evaluations are widely consistent with microscopy pictures published in the literature.

6.2 Outlook

As mentioned in the introduction, this thesis is the second one in a series of three. The third thesis in this project will combine the elasto-plastic material approach with the cohesive zone crack model of Clemens Reichel to allow a comprehensive evaluation of the indentation fracture mechanism of such a wafer structure. It is of great interest to study the influence of plasticity on crack initiation and propagation.

Regarding the modeling approach for single crystal plasticity, further studies will help to assess its full potential. For example, a closer look should be taken on the plastic strain development in the slip directions to examine the predictive capabilities of plastic single crystal deformations.

Finally, it is interesting to apply this modeling strategy to a different experimental setup or to another single crystal material and to compare it to a classical crystal plasticity simulation approach.

Appendix A

Rotation Convention and Schmid Factor Table

The Schmid factors calculation procedure and the final results for all of the slip systems of GaN are presented in the following. As explained in Chapter 3.1, the transformation

$$\underline{\underline{R}}\,\underline{\underline{\sigma}}\,\underline{\underline{R}}^T = \begin{pmatrix} \sigma_{x'x'} & \tau_{x'y'} & \tau_{x'z'} \\ & \sigma_{y'y'} & \tau_{y'z'} \\ sym. & & \sigma_{z'z'} \end{pmatrix} \tag{A.1}$$

is used to calculate the Schmid factors of the various slip system. For most systems, rotations around two axes are necessary to perform the transformation between the local and the global coordinate systems. Solely to calculate the Schmid factor of the $\{1\bar{1}01\}\langle 11\bar{2}3\rangle$ slip system a third rotation is needed. The z-$\tilde{y}$-$\tilde{\tilde{z}}$ Euler angle sequence

$$\underline{\underline{R}} = \begin{pmatrix} c(\alpha)c(\beta)c(\gamma) - s(\alpha)s(\gamma) & -s(\alpha)c(\beta)c(\gamma) - c(\beta)s(\gamma) & s(\alpha)c(\gamma) \\ c(\alpha)c(\beta)s(\gamma) + s(\alpha)c(\gamma) & -s(\alpha)c(\beta)s(\gamma) + c(\alpha)c(\gamma) & s(\beta)s(\gamma) \\ -c(\alpha)s(\beta) & s(\alpha)s(\beta) & c(\beta) \end{pmatrix} \tag{A.2}$$

c() ... cos() α ...first rotation around the z-axis

s() ... sin() β ...second rotation around the $\tilde{y}$-axis

                                γ ...third rotation around the $\tilde{\tilde{z}}$-axis

is chosen as rotation convention. The orientations of the slip systems of GaN are described by the rotation angles presented in Table A.1. The angle α describes the rotation around the $\langle 0001 \rangle$ axis and β the inclination towards the basal plane. The third rotation γ is only used for the $\{1\bar{1}01\}\langle 11\bar{2}3 \rangle$ slip system and characterizes the two possible orientations of the $\langle 11\bar{2}3 \rangle$ direction. For each slip plane three angles α have to be considered, due to the six-folded symmetry of the GaN crystal.

These rotation angles are used to transform the stress tensor $\underline{\underline{\sigma}}$ into a coordinate system ( )$'$ in which the z'-axis is perpendicular to the slip plane and the y' and x'-axis point in the slip directions. The two slip direction are orthogonal for the $\{\bar{1}2\bar{1}0\}$, the $\{1\bar{1}00\}$, the $\{11\bar{2}2\}$, and the $\{1\bar{1}02\}$ plane. Thus, the Schmid factors for a uniaxial stress σ_{ii} $(i = x, y, z)$, are then equal the transformed shear stresses $\tau_{x'z'}$ and $\tau_{y'z'}$. The shear stress $\tau_{y'z'}$ is hereby the Schmid factor of the slip direction in the basal plane and $\tau_{x'z'}$ is the Schmid factor of the second slip direction ($\langle 0001 \rangle$, $\langle 11\bar{2}3 \rangle$ or $\langle 1\bar{1}01 \rangle$).

Table A.1: Rotation angles for the slip systems of GaN.

Slip plane	α	β	γ
$\{0001\}$	$0°$	$0°, 60°, 120°$	
$\{\bar{1}2\bar{1}0\}$	$90°$	$0°, 60°, 120°$	
$\{1\bar{1}00\}$	$90°$	$30°, 90°, 150°$	
$\{1\bar{1}01\}$	$62.0°$	$30°, 90°, 150°$	$(\pm 15.74°)$
$\{11\bar{2}2\}$	$58.4°$	$0°, 60°, 120°$	
$\{1\bar{1}02\}$	$43.2°$	$30°, 90°, 150°$	

In case of the $\{1\bar{1}01\}$ slip plane, the two sliding directions are not orthogonal to each other and therefore have to be considered separately. The Schmid factors of the $\langle\bar{1}2\bar{1}0\rangle$ direction are calculated without the third rotation γ. However, for the slip direction $\langle11\bar{2}3\rangle$ the two possible orientations have to be evaluated using the third rotation $\gamma = \pm15.74°$. The corresponding Schmid factors are then equal $\tau_{x'z'}$. The highest and therefore critical Schmid factors of each slip system are presented in Table A.2.

Table A.2: Schmid factors for all slip systems and uniaxial stresses in the global coordinate system. The values for the Peierls-Nabarro stresses $\tau_{\text{PN}}^{\text{Y}}$ are taken from [2] and the experimental uniaxial compression yield stress $\sigma_{\text{exp}}^{\text{Y}}$ is taken from [30].

Slip system		Load	Schmid factor	$\tau_{\text{PN}}^{\text{c}}$[GPa]	$\sigma_{\text{PN}}^{\text{Y}}$[GPa]	$\sigma_{\text{exp}}^{\text{Y}}$[GPa]
$\{0001\}$	$\langle\bar{1}2\bar{1}0\rangle$	σ_{xx}	0	2.34		
$\{\bar{1}2\bar{1}0\}$	$\langle0001\rangle$	σ_{xx}	0	16.5		
		σ_{yy}	0	16.5		
		σ_{zz}	0	16.5		
	$\langle1\bar{1}00\rangle$	σ_{xx}	0.433	19.7	45.5	
		σ_{yy}	0.433	19.7	45.5	
		σ_{zz}	0	19.7		
$\{1\bar{1}00\}$	$\langle0001\rangle$	σ_{xx}	0	10.4		
		σ_{yy}	0	10.4		
		σ_{zz}	0	10.4		
	$\langle\bar{1}2\bar{1}0\rangle$	σ_{xx}	0.433	1.21	2.79	
		σ_{yy}	0.433	1.21	2.79	
		σ_{zz}	0	1.21		
$\{1\bar{1}01\}$	$\langle11\bar{2}3\rangle$	σ_{xx}	0.402	54.7	136.06	
		σ_{yy}	0.399	54.7	137.09	
		σ_{zz}	0.399	54.7	137.09	7.85
	$\langle\bar{1}2\bar{1}0\rangle$	σ_{xx}	0.382	11.3	29.58	
		σ_{yy}	0.382	11.3	29.58	
		σ_{zz}	0	11.3		
$\{11\bar{2}2\}$	$\langle11\bar{2}3\rangle$	σ_{xx}	0.446	29.8	66.16	
		σ_{yy}	0.335	29.8	88.95	
		σ_{zz}	0.446	29.8	66.16	7.85
	$\langle1\bar{1}00\rangle$	σ_{xx}	0.369	23.3	63.14	
		σ_{yy}	0.369	23.3	63.14	
		σ_{zz}	0	23.3		
$\{1\bar{1}02\}$	$\langle1\bar{1}01\rangle$	σ_{xx}	0.374	85.3	228.07	
		σ_{yy}	0.499	85.3	170.94	
		σ_{zz}	0.499	85.3	170.94	7.85
	$\langle\bar{1}2\bar{1}0\rangle$	σ_{xx}	0.296	15.2	51.35	
		σ_{yy}	0.296	15.2	51.35	
		σ_{zz}	0	15.2		

Bibliography

[1] ANSYS, Inc. *ANSYS Academic Research Mechanical, Release 18.1, Mechanical APDL Theory Guide.*

[2] P. G. Caldas, E. M. Silva, R. Prioli, J. Y. Huang, R. Juday, A. M. Fischer, and F. A. Ponce. Plasticity and optical properties of gan under highly localized nanoindentation stress fields. *Journal of Applied Physics*, 121(12):125105, 2017.

[3] T. Daxner and F. Rammerstorfer. *Nichtlineare Finite Elemente Methoden Skriptum.* ILSB, Wien, 2015.

[4] E. Dobrovinskaya, L. Lytvynov, and V. Pishchik. *Sapphire: Material, Manufacturing, Applications.* Micro- and Opto-Electronic Materials, Structures, and Systems. Springer US, 2009.

[5] S. Evtimova, B. Arnaudov, T. Paskova, B. Monemar, and M. Heuken. Effect of carrier concentration on the microhardness of gan layers. *Journal of Materials Science: Materials in Electronics*, 14(10):771–772, Oct 2003.

[6] J. Hay. Introduction to instrumented indentation testing. *Experimental Techniques*, 33(6):66–72, 2009.

[7] R. Hertzberg. *Deformation and fracture mechanics of engineering materials.* Wiley, 1989.

[8] R. Hill. *The Mathematical Theoryof Plasticity.* Oxford University Press, USA, 1950.

[9] D. Holt and B. Yacobi. *Extended Defects in Semiconductors: Electronic Properties, Device Effects and Structures*. Cambridge University Press, 2007.

[10] M. A. Hopcroft, W. D. Nix, and T. W. Kenny. What is the young's modulus of silicon? *Journal of Microelectromechanical Systems*, 19(2):229–238, April 2010.

[11] J. Huang, K. Xu, X. J. Gong, J. F. Wang, Y. M. Fan, J. Q. Liu, X. H. Zeng, G. Q. Ren, T. F. Zhou, and H. Yang. Dislocation cross-slip in gan single crystals under nanoindentation. *Applied Physics Letters*, 98(22):221906, 2011.

[12] R. Iankov, M. Datcheva, S. Cherneva, and D. Stoychev. Finite element simulation of nanoindentation process. In I. Dimov, I. Faragó, and L. Vulkov, editors, *Numerical Analysis and Its Applications*, pages 319–326, Berlin, Heidelberg, 2013. Springer Berlin Heidelberg.

[13] S. Imaoka. Hill's potential. `http://www.cae-wiki.info/wikiplus/images/8/89/STI0808_Hill.pdf`, 2008. Accessed: 2017-12-5.

[14] Infineon Technologies AG. Infineon unveils portfolio of energy-efficient enhancement mode and cascode configuration gan-on-silicon platforms at apec 2015. `https://www.infineon.com/dgdl/Infineon-PressRelease_GalliumNitride-AP-v01_00-EN.pdf?fileId=5546d4624bcaebcf014c26ffdf215a2e`, 2015. Accessed: 2017-11-24.

[15] S.-R. Jian, T.-H. Fang, and D.-S. Chuu. Analysis of physical properties of iii-nitride thin films by nanoindentation. *Journal of Electronic Materials*, 32(6):496–500, Jun 2003.

[16] J. Kim, D.-i. D. Cho, and R. S. Muller. *Why is (111) Silicon a Better Mechanical Material for MEMS?*, pages 662–665. Springer Berlin Heidelberg, Berlin, Heidelberg, 2001.

[17] C. Kittel. *Introduction to Solid State Physics*. John Wiley & Sons, Inc, USA, 8 edition, 2005.

[18] S. O. Kucheyev, J. E. Bradby, J. S. Williams, C. Jagadish, M. Toth, M. R. Phillips, and M. V. Swain. Nanoindentation of epitaxial gan films. *Applied Physics Letters*, 77(21):3373–3375, 2000.

[19] M. Lichinchi, C. Lenardi, J. Haupt, and R. Vitali. Simulation of berkovich nanoindentation experiments on thin films using finite element method. *Thin Solid Films*, 312(1):240 – 248, 1998.

[20] N. Nakamura, H. Ogi, and M. Hirao. Elastic, anelastic, and piezoelectric coefficients of gan. *Journal of Applied Physics*, 111(1):013509, 2012.

[21] R. Nowak, M. Pessa, M. Suganuma, M. Leszczynski, I. Grzegory, S. Porowski, and F. Yoshida. Elastic and plastic properties of gan determined by nanoindentation of bulk crystal. *Applied Physics Letters*, 75(14):2070–2072, 1999.

[22] K. E. Petersen. Silicon as a mechanical material. *Proceedings of the IEEE*, 70(5):420–457, May 1982.

[23] A. Polian, M. Grimsditch, and I. Grzegory. Elastic constants of gallium nitride. *Journal of Applied Physics*, 79(6):3343–3344, 1996.

[24] M. Reisinger, J. Zalesak, R. Daniel, M. Tomberger, J. Weiss, A. Darbal, M. Petrenec, J. Zechner, I. Daumiller, W. Ecker, B. Sartory, and J. Keckes. Crosssectional stress distribution in alxga1-xn heterostructure on si(111) substrate characterized by ion beam layer removal method and precession electron diffraction. *Materials & Design*, 106(Supplement C):476 – 481, 2016.

[25] E. Schmid and W. Boas. *Kristallplastizität, mit besonderer Berücksichtigung der Metalle*. Struktur und Eigenschaften der Materie. Edwards Brothers, 1935.

[26] R. B. Schwarz, K. Khachaturyan, and E. R. Weber. Elastic moduli of gallium nitride. *Applied Physics Letters*, 70(9):1122–1124, 1997.

[27] C.-H. Tsai, S.-R. Jian, and J.-Y. Juang. Berkovich nanoindentation and deformation mechanisms in gan thin films. *Applied Surface Science*, 254(7):1997 – 2002, 2008.

[28] J. J. Vlassak and W. Nix. Measuring the elastic properties of anisotropic materials by means of indentation experiments. *Journal of the Mechanics and Physics of Solids*, 42(8):1223 – 1245, 1994.

[29] T. Wei, Q. Hu, R. Duan, J. Wang, Y. Zeng, and J. Li. Mechanical deformation behavior of nonpolar gan thick films by berkovich nanoindentation. *Nanoscale Research Letters*, 4(7):753–757, 2009.

[30] J. Wheeler, C. Niederberger, C. Tessarek, S. Christiansen, and J. Michler. Extraction of plasticity parameters of gan with high temperature, in situ microcompression. *International Journal of Plasticity*, 40:140 – 151, 2013.

[31] G. Yu, H. Ishikawa, T. Egawa, T. Soga, J. Watanabe, T. Jimbo, and M. Umeno. Mechanical properties of the gan thin films deposited on sapphire substrate. *Journal of Crystal Growth*, 189-190:701–705, 1998. cited By 40.